



A comprehensive assessment of in situ and remote sensing soil moisture data assimilation in the APSIM model for improving agricultural forecasting across the US Midwest

Marissa Kivi¹, Noemi Vergopolan², and Hamze Dokoohaki¹

¹Department of Crop Sciences, University of Illinois at Urbana-Champaign, Urbana, IL, USA

²Department of Civil and Environmental Engineering, Princeton University, Princeton, NJ, USA

Correspondence: Hamze Dokoohaki; hamzed@illinois.edu

Received: 29 September 2022 – Discussion started: 25 October 2022

Revised: 31 January 2023 – Accepted: 6 February 2023 – Published: 16 March 2023

Abstract. Today, the most popular approaches in agricultural forecasting leverage process-based crop models, crop monitoring data, and/or remote sensing imagery. Individually, each of these tools has its own unique advantages but is, nonetheless, limited in prediction accuracy, precision, or both. In this study we integrate in situ and remote sensing (RS) soil moisture observations with APSIM model through sequential data assimilation to evaluate the improvement in model predictions of downstream state variables across five experimental sites in the US Midwest. Four RS data products and in situ observations spanning 19 site years were used through two data assimilation approaches, namely ensemble Kalman filter (EnKF) and generalized ensemble filter (GEF), to constrain model states at observed time steps and estimate joint background and observation error matrices. Then, the assimilation's impact on estimates of soil moisture, yield, normalized difference vegetation index (NDVI), tile drainage, and nitrate leaching was assessed across all site years. When assimilating in situ observations, the accuracy of soil moisture forecasts in the assimilation layers was improved by reducing RMSE by an average of 17 % for 10 cm and ~ 28 % for 20 cm depth soil layer across all site years. These changes also led to improved simulation of soil moisture in deeper soil layers by an average of 12 %. Although crop yield was improved by an average of 23 %, the greatest improvement in yield accuracy was demonstrated in site years with higher water stress, where assimilation served to increase available soil water for crop uptake. Alternatively, estimates of annual tile drainage and nitrate leaching were not well constrained across the study sites. Trends

in drainage constraint suggest the importance of including additional data constraint such as evapotranspiration. The assimilation of RS soil moisture showed a weaker constraint of downstream model state variables when compared to the assimilation of in situ soil moisture. The median reduction in soil moisture RMSE for observed soil layers was lower, on average, by a factor of 5. However, crop yield estimates were still improved overall with a median RMSE reduction of 17.2 %. Crop yield prediction was improved when assimilating both in situ and remote sensing soil moisture observations, and there is strong evidence that yield improvement was higher when under water-stressed conditions. Comparisons of system performance across different combinations of remote sensing data products indicated the importance of high temporal resolution and accurate observation uncertainty estimates when assimilating surface soil moisture observations.

1 Introduction

To effectively address pressing global food security challenges, agricultural forecasting tools must exhibit high accuracy and precision across spatial and temporal scales. As process-based crop models offer a system-level representation of many soil and crop processes, they are increasingly recognized as practical forecasting tools in agricultural research (Silva and Giller, 2021; Fer et al., 2021). However, their weakness comes from many unaccounted uncertainties, such as those related to model parameters, initial con-

ditions, and weather (Dokoohaki et al., 2021). Prior studies have shown state data assimilation (SDA) to be a powerful tool to overcome this weakness in process-based crop models (e.g., Dokoohaki et al., 2022a). SDA enables a temporally continuous, high-dimensional scaffold in which a variety of observations can be smoothly integrated using one of many robust, systematic algorithms, such as the ensemble Kalman filter (EnKF; Dietze, 2017; Huang et al., 2019; Liu et al., 2021; Dokoohaki et al., 2022a; Kivi et al., 2022). Through SDA, uncertainty around spatially heterogeneous and dynamic properties in agricultural systems can be constrained, thereby increasing precision and accuracy in estimates while decreasing dependence on extensive site-level model calibration (Mishra et al., 2021).

Numerous past studies have used SDA to constrain crop model estimates, using observations on leaf area index (e.g., Nearing et al., 2012; Ines et al., 2013; Ma et al., 2013; Chen et al., 2018; Lu et al., 2021), soil moisture (Kivi et al., 2022), biomass (e.g., Linker and Ioslovich, 2017), and evapotranspiration (e.g., Huang et al., 2015). For example, a synthetic study by Zhu et al. (2017) found that the assimilation of coarse-resolution surface soil moisture data into a coupled soil water–groundwater numerical model constrained soil moisture estimates in the first 50 cm of the soil profile despite explicitly unaccounted spatial heterogeneity in soil properties. These studies showed how SDA can partially account for the spatial variability in soil hydraulic conductivity across broad regions without explicit model calibration. In addition to incorporating spatial heterogeneity in soil properties, Kivi et al. (2022) demonstrated that the assimilation of high-quality and frequent in situ soil moisture observations can substantially improve downstream model predictions of tile drainage, nitrate (NO_3) leaching, and root zone soil moisture (RZSM) for maize and soybeans in the APSIM model. However, collecting field measurements of soil moisture for different cropping systems, soils, and environments is expensive, extremely laborious, and time-consuming.

Alternatively, the assimilation of high-resolution remote sensing (RS) data products dramatically increases SDA applications' range beyond in situ data availability by effectively capturing the spatiotemporal variability of many agricultural state variables, such as vegetation cover and soil moisture, with consistency and high temporal frequency (Peng et al., 2017). As a result, RS observations could be invaluable to constraining model predictions at the regional scale and have been increasingly applied for agricultural forecasting in the data assimilation literature, as demonstrated in literature reviews by Dorigo et al. (2007), Huang et al. (2019), and Weiss et al. (2020). The application of RS soil moisture data products has been especially popular and successful in data-assimilation-focused agricultural forecasting studies. These data products, which characterize soil moisture content in the first 5 cm of the soil profile, pull information from active and/or passive sensors of microwave reflectance. Due its high sensitivity to surface soil

moisture, many data products have been developed around available L-band microwave sensor information collected by NASA's SMAP Mission (Kumar et al., 2018). The SMAP–HydroBlocks (SMAP–HB) data products merges SMAP data with the HydroBlocks land surface model to increase spatial resolution in the final estimates and improve scalability (Vergopolan et al., 2021b), while the SMAP–Sentinel1 data product pairs SMAP data with Sentinel-1 radar information to achieve similar goals (Das et al., 2019). Others, like the ESA CCI data product (Dorigo et al., 2017), compile information from multiple sensors, including the SMAP passive sensor, to allow for greater temporal coverage. However, this approach comes at the cost of coarser spatial resolution.

Nonetheless, as demonstrated in past studies, the assimilation of RS soil moisture data has its limitations. First, uncertainty and biases in RS data products are typically poorly defined (Huang et al., 2019). RS-based data products are based on empirical relationships, and, as they are predicted as a function of surface reflectance, uncertainties in the raw radiance will propagate unsupervised into final estimates (Weiss et al., 2020). Additionally, RS estimates characterize soil moisture in only the top 5 cm of the soil profile and, thus, rely on models or empirical parameterizations to describe the root zone soil profile. Among others, de Lannoy et al. (2007) and Monsivais-Huertero et al. (2010) both found the assimilation of in situ near-surface soil moisture observations to be far less effective than that of in situ RZSM observations in constraining estimates of the greater soil water profile. Yet, since the surface layer is typically the layer where fertilizers are added, the accurate estimation of surface layer state variables is essential for today's agroecosystems. To overcome relatively coarse spatial resolution in RS data products, past studies have explored downscaling approaches (e.g., Chakrabarti et al., 2014) or leveraged additional in situ datasets (e.g., Liu et al., 2021) to overcome “mismatch” challenges and downscale RS soil moisture estimates to more accurately reflect field scale measurements (Vergopolan et al., 2021a). However, the reliance on in situ observations of these approaches can limit system transferability across broad regions (Peng et al., 2017). Moreover, as described by Crow et al. (2012), it can be difficult to properly evaluate coarse-resolution soil moisture estimates with point-scale ground measurements due to unknown and often significant sampling uncertainty. Data assimilation with process-based models has been previously applied as a robust and scalable way to leverage information in coarse-resolution soil moisture estimates (e.g., Vergopolan et al., 2021b).

Despite the immense theoretical potential of SDA with both in situ and RS observations, past studies have reported inconsistent SDA performance in modeling crop yields. For example, de Wit and van Diepen (2007) observed inconsistencies in yield constraint when assimilating soil wetness index (SWI) derived from 0.25° ERS1/2 microwave radiance information into the WOFOST model across agricultural regions of Spain, Germany, France, and Italy. They partially at-

tributed poor predictions in certain regions to irrigation processes that were captured neither by the model nor by coarse-resolution SWI observations. Lu et al. (2021) also saw year-to-year variability in assimilation performance when assimilating in situ observations of canopy cover and soil moisture for 6 site years in Nebraska. When assimilating soil moisture independently, canopy cover estimates were better constrained in drier years. They suspected this to result from the canopy cover's lower sensitivity to soil moisture in the model when water is in surplus (i.e., due to energy-limited conditions). We further suspect that SDA's inconsistent performance is related to the misrepresentation of model processes linking soil moisture to crop- and soil-related variables (e.g., soil nitrogen, leaf expansion, crop water uptake). As a result, direct upstream improvement of model state variables with SDA does not always translate into improvement in downstream results. To understand the role of soil moisture data assimilation in improving crop yields and better pinpoint areas for future improvement, a comprehensive assessment that investigates performance across time and different genetic (G), environmental (E), and management (M) spaces is required. Although a growing body of studies has attempted to quantify the impact of soil moisture assimilation in crop models, such a comprehensive evaluation of in situ and RS soil moisture SDA in crop models across GxExM spaces is still lacking (Folberth et al., 2016).

To bridge this knowledge gap, we present a comprehensive assessment of soil moisture data assimilation as a method for constraining crop model predictions across the US Midwest. Building on the assimilation framework in Kivi et al. (2022), we independently assimilated both in situ and RS soil moisture observations in the APSIM crop model at five experimental sites in the US Midwest. With field data covering 19 site years of corn and soybean cropping systems across the region, this study tests the data assimilation system across a broader GxExM inference space and quantifies the benefit of assimilating different RS soil moisture products in comparison to the in situ soil moisture observations. The main objectives of this study were

1. to quantify how in situ soil moisture observations can constrain crop model forecasts of downstream estimates, including RZSM, crop yield, crop phenology via normalized difference vegetation index (NDVI), tile drainage flow, and NO_3 leaching through SDA;
2. to quantify the added benefit of RS soil moisture observations in improving crop model predictions of RZSM, crop yield, and crop phenology via NDVI through SDA.

2 Methods

Section 2.1 and 2.2 describe the five experimental sites and the in situ observations employed in this study for model setup, SDA, and evaluation. Section 2.3 outlines the four dif-

ferent RS soil moisture data products that were assimilated, and Sect. 2.4 presents the data-assimilation system used in this study. Lastly, Sect. 2.4.5 defines the different simulation experiments performed.

2.1 Study sites

This study focused on five experimental sites across the US Midwest with in situ observations of soil moisture, crop yield, nitrate load, and tile drainage flow for 19 sites \times years between 2011 and 2019. Site IL was the Energy Farm, a well-monitored experimental site in central Illinois that was the focus of the development and initial evaluation of the employed data-assimilation system (Kivi et al., 2022). Sites IN, MN, OH, and SD were available through the Transforming Drainage (TD) project (Chighladze et al., 2021). The TD project database is publicly available and contains high-quality data from 39 tile-drained research sites with data spanning over 200+ site years. The available observations include data on tile drainage, yield, water table, water quality, and soil characteristics, among many others. Though numerous sites were available as part of the project, the experimental design and data available for each site year vary widely in the database. For consistency, this work required that each site year include a plot with (1) a free tile drainage system, (2) available NO_3 load and tile flow data at the plot level, (3) available in situ soil moisture observations, (4) maize or soybean crops, and (5) a rain-fed system. We identified only 17 site years across five sites in the database which satisfied all these criteria.

To properly set up the APSIM model for each of the five sites, we included all available site information on each year, cropping system, residue type, planting and harvesting details, tillage practices, and fertilizer applications as constants in the simulations. Following updated information available through Moore et al. (2021), the IL site includes tillage practices in the model setup and increased nitrogen (N) fertilizer from 64.6 to 202 kg N ha⁻¹. Detailed information on the plot and management information for all five sites are included in Table A1. Study sites will be referred to by their given study IDs in Fig. 1.

2.2 Observation data

2.2.1 In situ soil moisture

Across the study site years, subdaily soil moisture (SM) observations were collected at various soil depths between 10 and 105 cm using soil sensors; the measured depths and sensor type varied by site. All observations are available in units of volumetric water fraction (VFW; mm mm⁻¹). For the four TD sites, SM observations were only available as daily averages. For consistency, SM observations at IL (available at 15 min intervals) were aggregated to daily averages when at least forty 15 min observations were available. Ob-

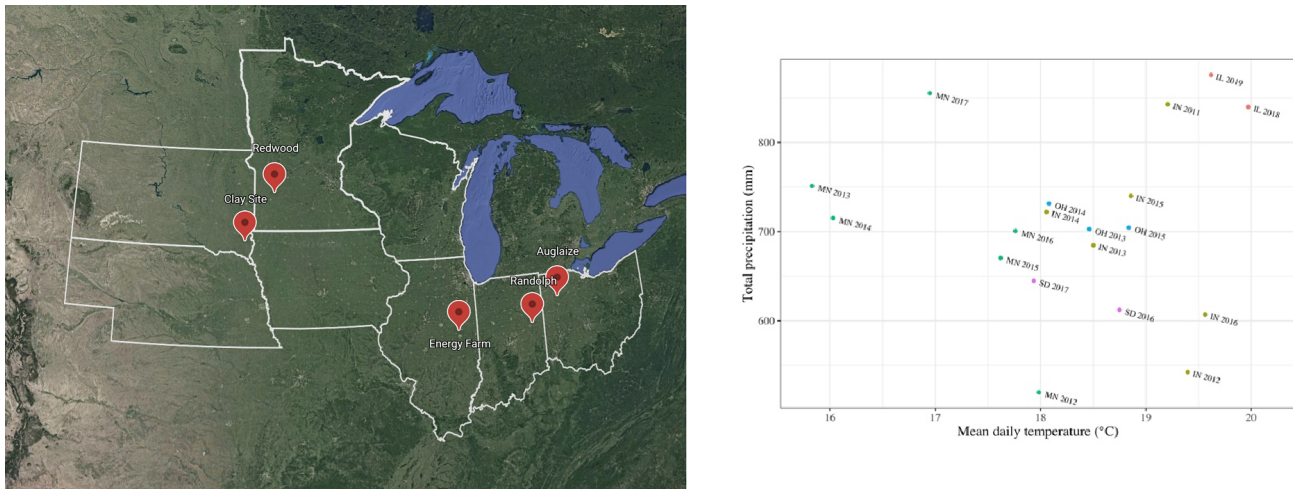


Figure 1. Left: site map (ESRI). Right: scatterplot demonstrating site-year total precipitation and average daily temperature ($^{\circ}\text{C}$) for each site year between April and October. Climate information was extracted and averaged across the 10 ERA5 weather ensembles for each site year.

servations from the winter months (December–March) were excluded due to the influence of freezing soils. Across all site years, in situ SM assimilation was performed with available observations for the 10 and 20 cm soil depths, which hereinafter will be referred to as SM3 and SM4, respectively. All other available SM observations for deeper soil layers were used to evaluate model RZSM estimates. SM observations were paired with an APSIM soil layer based on the recorded sensor depth and the site soil profile. In the case that more than one observation was available for a given APSIM soil layer, the average SM was computed for each day and layer with the assumption of uniform SM in the layer.

2.2.2 Harvested maize and soybean yields

Data on harvested yield for the TD sites were available for each site year with 1–3 replicated measurements. These replicated observations were averaged and converted from grain at standard moisture content (i.e., 15.5% for maize and 13% for soybean) to dry-grain weight for best comparison with the APSIM model output. Observations for IL were already recorded as dry-grain weights and given in units of kg ha^{-1} . Across 12 maize site years, observed yields ranged from 6.51 to 13 mg ha^{-1} with an average yield of 9.93 mg ha^{-1} . The 7 soybean site years had observed yields ranging from 2.78 to 4.15 mg ha^{-1} with an average yield of 3.50 mg ha^{-1} .

2.2.3 Remotely sensed normalized difference vegetation index (NDVI)

The normalized difference vegetation index (NDVI) can be used to quantify vegetation greenness and reasonably track the phenological development of crops (Gao and Zhang,

2021). In this study, NDVI observations from Landsat between 2011 and 2019 were used to evaluate APSIM's performance in predicting crop phenology for each site year. NDVI time series were extracted at each site location from Landsat 7 and 8 remote sensing imagery courtesy of the US Geological Survey via Google Earth Engine and derived from the red (RED) and near-infrared (NIR) spectral bands using the following equation:

$$\text{NDVI} = \frac{\text{NIR} - \text{RED}}{\text{NIR} + \text{RED}} \quad (1)$$

2.2.4 In situ measurements of tile drainage and nitrate load

Daily observations of tile drainage flow (mm) and NO_3 load ($\text{kg NO}_3 \text{N ha}^{-1}$) were available for all 19 site years. Any missing daily drainage values for the TD sites had been imputed previously and used to approximate missing values of daily NO_3 load, as described by Helmers et al. (2022). Methods and instrumentation used to collect and process the TD sites and IL data are presented by Helmers et al. (2022) and Kivi et al. (2022), respectively. In this study, daily values for tile drainage flow and NO_3 load were summed to annual values for comparison with model output. For the purposes of this analysis, we assumed any day with NA tile drainage flow values in the data had no drainage and no NO_3 loss.

2.3 Remote sensing soil moisture

To assess the performance of SM data assimilation with satellite-based observations, we included four RS data products that span different temporal and spatial resolutions (Table 1). These observations were extracted at the point level for the study sites and serve to represent the first 5 cm of

Table 1. Overview of remote sensing soil moisture data products.

Product	Product ID	Temporal coverage	Temporal frequency	Spatial resolution	Average data availability*	Average observation variance	Reference
ESA CCI	ESA	1978–2019	1–2 d	0.25°	219 d	0.0003	Dorigo et al. (2017)
SMAP–HydroBlocks	SMAP–HB	2015–2019	1–3 d	30 m	127 d	0.0050	Vergopolan et al. (2021b)
SMAP–Sentinel1	1/3 km	2015–now	12 d	1/3 km	7 d	0.0025	Das et al. (2019)

* Availability is calculated after removing observations in the winter months (i.e., December–March) and is given on a per-year basis.

the soil profile or surface SM. Observations from the winter months (i.e., December–March) were removed to avoid issues with snow cover and freezing soils. The product IDs provided in Table 1 will be used to identify each data product.

2.3.1 ESA CCI

The RS dataset with the coarsest spatial resolution in this study was the European Space Agency Climate Change Initiative (ESA CCI) SM product. Each year, the ESA CCI algorithmically merges information from 3 active (e.g., ASCAT A/B) and 10 passive (e.g., SSM/I, AMSR-E, SMOS, SMAP) microwave sensors to estimate daily surface SM globally for over 40 years. Dorigo et al. (2017) provide complete documentation on how these data products are produced. Here we used the combined product (version v06.1), which includes daily uncertainty estimates. Several past studies have assimilated this data product into process-based models with varying levels of success (e.g., Zhou et al., 2016; Liu et al., 2017, 2018; Naz et al., 2019).

2.3.2 SMAP–HydroBlocks

The SMAP–HydroBlocks surface SM dataset has the highest spatial resolution in this study. It was introduced by Vergopolan et al. (2021b) by combining the HydroBlocks land surface model, a tau–omega radiative transfer model, machine learning, in situ SM observations, and SMAP remotely sensed satellite observations to estimate surface SM with 30 m resolution across the contiguous United States. Specifically, the HydroBlocks model was coupled with a tau–omega radiative transfer model (HydroBlocks–RTM) and used to simulate SM, soil temperature, and brightness temperature at a 3 h, 30 m resolution. Brightness temperature estimates from NASA’s Soil Moisture Active Passive (SMAP) mission were then merged with the HydroBlocks–RTM estimates using a spatial cluster-based Bayesian merging scheme (Vergopolan et al., 2020). Using the inverse HydroBlocks–RTM, SM was estimated at SMAP overpass time at 30 m spatial resolution. Vergopolan et al. (2021b) reported an RMSE of $0.07 \text{ mm}^3 \text{ mm}^{-3}$ after comparing SMAP–HydroBlocks estimates to in situ observations from 233 independent experimental sites. This study is the first to assimilate SMAP–HydroBlocks SM estimates into a crop model. SM morn-

ing and afternoon retrievals were aggregated to a daily resolution, and site-level estimates were computed as the mean value of any data point within 0.0005° of the given site location. The uncertainty estimate for each observation was calculated based on the spatial variability of selected data points for that time step and the reported standard error ($\text{SE} = 0.07 \text{ mm}^3 \text{ mm}^{-3}$) as

$$\text{Var}(Y_{s,t}) = \text{Var}(y_t) + \text{SE}^2, \quad (2)$$

where, for site s at the t th available time step, Y represents the site-level SM estimate, and y presents SM estimates within 0.0005° of the site location.

2.3.3 SMAP–Sentinel1

The SMAP–Sentinel1 SM product was produced by merging information collected by the SMAP L-band radiometer and the Copernicus Project Sentinel-1 C-band radar. After the malfunction of the SMAP radar in 2015, Sentinel-1 active microwave data were used with passive microwave sensor information from the still-operating SMAP radiometer to estimate surface SM content globally using the active–passive algorithm. Although the merged product increased the revisit interval from 3 to 12 d, it enabled retrievals at two different spatial resolutions (i.e., 1 and 3 km; Lievens et al., 2017). Upon comparing the estimates with in situ SM measurements, Das et al. (2019) reported RMSE for SMAP–Sentinel1 SM estimates as roughly $0.05 \text{ m}^3 \text{ m}^{-3}$. In this study, this value was applied as the standard error for SM estimates at both spatial resolutions and at all available time steps. Retrievals were available for all TD site years but were unavailable for IL for unknown reasons.

2.4 Data-assimilation system

This study uses the data-assimilation system developed and evaluated in Kivi et al. (2022). The original system leveraged the pSIMS platform, APSIM crop model, ensemble Kalman filter (EnKF), and an algorithm presented by Miyoshi et al. (2013) to estimate and propagate uncertainties, perform sequential data assimilation, and generate daily agricultural forecasts at the field scale. The workflow is illustrated in Fig. 2. APSIM management variables that were known include planting and harvest dates, fertilizer amount, type, and

timing, tillage type, depth, and timing, crop type, row spacing, sowing density, and, if available, planting depth.

2.4.1 Model parameter priors

Initial soil water, cultivar, and residue weight were randomized across model ensembles for each site to incorporate uncertainty around initial conditions. If unavailable in the management data, planting depth was also randomized and drawn from different prior distributions for each crop. These distributions represented reasonable planting depth ranges for the two crops in the Midwest, as described in extension websites produced by the University of Missouri (Luce, 2016) and Michigan State University (Staton, 2012). Using a uniform prior distribution, planting depths ranged from 1.5 to 2.5 in. (3.8–6.35 cm) for maize and 1 to 2 in. (2.5–5 cm) for soybean.

Prior distributions were also set to incorporate uncertainty around cultivar. For maize, nine cultivar parameters were grouped into an ensemble, including the six cultivar parameters (i.e., `tt_flower_to_maturity`, `tt_flower_to_start_grain`, `tt_maturity_to_ripe`, `tt_emerg_to_endjuv`, `head_grain_no_max`, `grain_gth_rate`). The other three parameters (i.e., `largestLeafParams1`, `leaf_init_rate`, `leaf_app_rate1`) were drawn from Dokoohaki et al. (2022b), who identified maize cultivar parameters that were influential for estimates of leaf area index (LAI) in the APSIM maize module and optimized their value distributions using a hierarchical Bayesian optimization approach across the US Midwest. Table A2 gives more detailed information on all randomized parameters and their prior distributions. We completed a preliminary assessment of the maize module at each of the study sites and found that, under the given parameter value ranges, APSIM was capable of appropriately simulating the phenological development and grain yield for maize at each site.

The selection of soybean cultivars for each site was determined using a semi-systematic approach. First, a range of maturity groups were determined for each site based on a study by Mourtzinis and Conley (2017), which delineated soybean maturity groups across the United States. We defined the upper and lower maturity group bounds for each site using the bounding zone contour lines for each site location in Fig. 4 of Mourtzinis and Conley (2017). Then, initial APSIM simulations were performed for each site using all APSIM-defined soybean cultivars falling within the prescribed maturity group range. The model results were compared to the observed soybean yields at each site, and the best-performing maturity group (MG) for each site was determined. The final range for each site was approximately $MG \pm 0.5$. In each ensemble, the cultivar for each crop at each site was assumed to be constant across all site years.

2.4.2 Weather and soil model drivers

To incorporate uncertainty around soil and weather into our simulations, a Monte Carlo sampling approach was used to randomly assign ensembles of weather and soil drivers to model ensembles. For each study site, 10 weather ensembles from the ERA5 reanalysis data product were employed to characterize solar radiation, maximum air temperature, minimum air temperature, precipitation, and wind speed at the daily resolution and at each site location. ERA5 is a global gridded reanalysis data product from the European Centre for Medium-Range Weather Forecasts (ECMWF), which characterizes the weather state variables at hourly time steps with associated uncertainties (Hersbach et al., 2020). In addition, 25 soil ensembles were generated from the SoilGrids global gridded soil database (Hengl et al., 2014) for each site location. These ensembles cover 30 soil properties (including available water lower limit, bulk density, drained upper limit, organic carbon, soil class, and pH) and were created by sampling from each soil parameter mean and uncertainty values available in the SoilGrids dataset.

2.4.3 PROSAIL model

Since APSIM does not currently estimate NDVI, APSIM was coupled with the PROSAIL model described in Dokoohaki et al. (2022b) to estimate daily NDVI values and enable the appropriate evaluation of the model's simulation of crop phenology at the study sites. The PROSAIL model is a radiative transfer tool that combines PROSPECT, a leaf optical properties model, and SAIL, a canopy bidirectional reflectance model, to estimate spectral reflectance for a given vegetative area based on soil and plant/canopy properties (Jacquemoud et al., 2009). In this study, APSIM's daily forecasts of soil and plant variables were transformed and used as inputs into the PROSAIL model to compute the spectral reflectance for each ensemble. Then, for each day and ensemble, the estimated spectral information was used to estimate NDVI using the vegetation index function within the `hsdar` R library (Lehnert et al., 2019). Further details on the coupling protocols can be found in Dokoohaki et al. (2022b).

2.4.4 Ensemble Kalman filter with the Miyoshi algorithm

The data-assimilation system (which we will call EnKF–Miyoshi hereinafter) employs the ensemble Kalman filter (EnKF) to assimilate SM observations into the APSIM model. The EnKF merges information from the model ensemble forecast distribution and observations (with associated uncertainty) at each time step to optimally estimate the state of the system (Evensen, 2003). The system also leverages the Miyoshi algorithm in series with the EnKF to improve estimates of the two system uncertainty matrices (i.e., \mathbf{P}_f and \mathbf{R}) and improve filter performance. Based on diagnos-

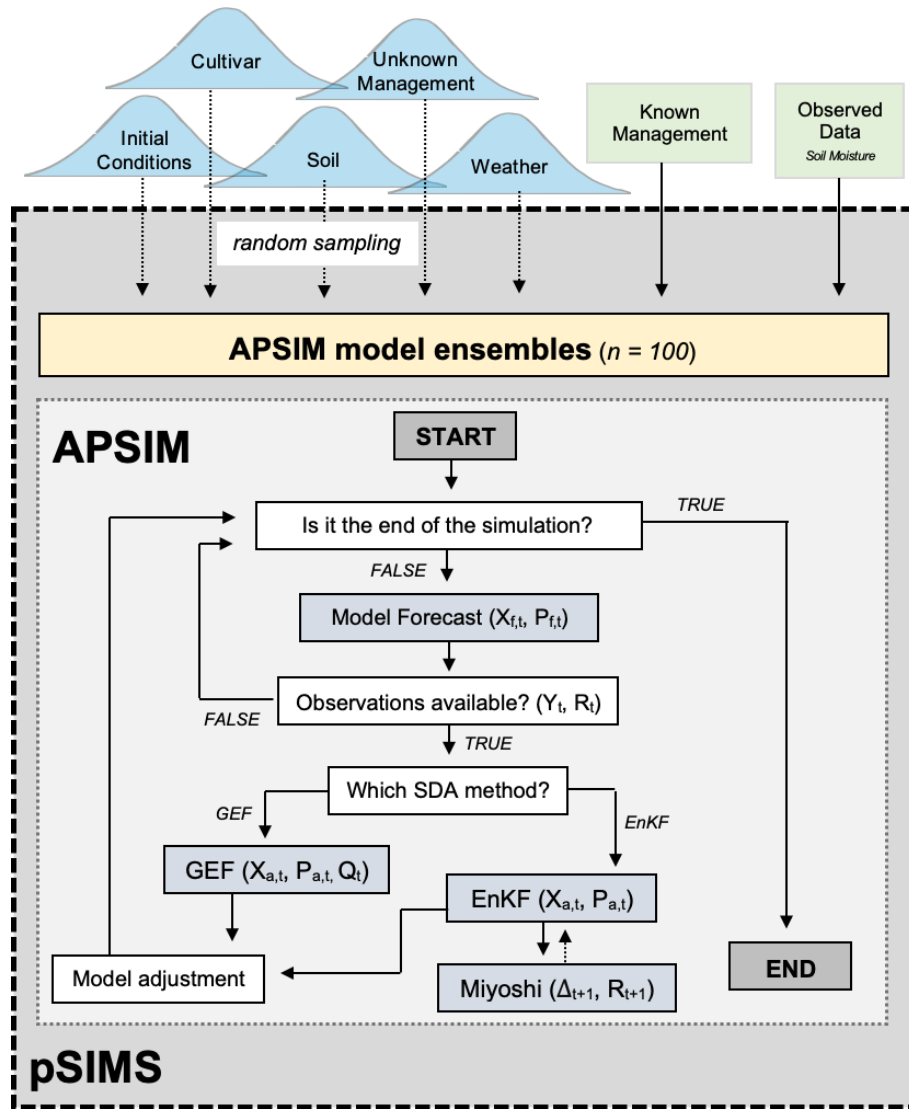


Figure 2. Schematic demonstrating the workflow of the data assimilation system. System inputs represented by blue normal distributions have incorporated uncertainty in this study, while green rectangles represent known values that were included as constants.

tic innovation statistics, the Miyoshi algorithm estimates a forecast inflation scalar (Δ) and observation uncertainty (R) at each analysis time step. At time step t with available data, the system follows the following steps:

1. The mean ($X_{f,t}$) and the variance–covariance matrix ($\mathbf{P}_{f,t}$) of the model forecast ensemble are computed to define the forecast distribution, which is assumed to follow a normal distribution.
2. The observed distribution (Y_t) is also assumed to be normal with mean y_t and variance–covariance matrix \mathbf{R}_t , where $\mathbf{R}_t = R^*$ from the previous analysis time step or $R_1 = \Sigma$. Σ is a diagonal matrix that assumes 10% standard error for each observed state variable.
3. The Kalman gain (K) is computed as follows, where $\Delta t = \Delta^*$ or $\Delta t = \mathbf{I}$ (\mathbf{I} is the identity matrix), and H is the observation operator:

$$K_t = \Delta_t P_{f,t} H^T (R_t + H \Delta_t P_{f,t} H^T)^{-1}. \quad (3)$$
4. The analysis distribution, which assumes a normal distribution, is determined with mean ($X_{a,t}$) and variance–covariance matrix ($\mathbf{P}_{a,t}$).

$$X_{a,t} = X_{f,t} + K_t (Y_t - H X_{f,t})$$

$$P_{a,t} = (\mathbf{I} - K_t H) P_{f,t} \quad (4)$$
5. The model ensemble is updated at each time step according to the analysis distribution based on each ensemble’s likelihood within the forecast distribution.

6. Δ^* and R^* are recomputed using the following series of equations, where d_{o-a} and d_{o-f} represent the observation-analysis and observation-forecast innovations for the current time step, respectively, E denotes the expectation operator, and ρ is a user-defined weight given to the new estimate. A lower bound of 1 is imposed on each entry in Δ_{est} , and only the diagonal entries of R_{est} are maintained.

$$\begin{aligned} E(d_{o-a}d_{o-f}^T) &= R_{\text{est}} \\ \Delta_{\text{est}} &= \frac{d_{o-f}^T d_{o-f} - R_{\text{est}}}{H \Delta_t P_{f,t} H^T} \\ R^* &= (\rho) R_{\text{est}} + (1 - \rho) R_t \\ \Delta^* &= (\rho) \Delta_{\text{est}} + (1 - \rho) \Delta_t \end{aligned} \quad (5)$$

2.4.5 Generalized ensemble filter

However, the EnKF–Miyoshi workflow as established cannot robustly handle observation operators (H) that change dimensions over time. However, to reduce information loss within the system, H must be able to adapt according to the number of observations available. To increase flexibility in system configuration, an alternative sequential data assimilation approach was tested in this work to replace the EnKF–Miyoshi method. The new method, hereinafter called the generalized ensemble filter (GEF), comprises a fully numerical Bayesian approach to estimating the analysis distribution and an inflation scalar. The model resembles the approach presented by Raiho et al. (2020) and Dokoohaki et al. (2022a) and has the following form at analysis time step t :

$$\begin{aligned} Q &\sim U(0.001, 5) \\ X_A &\sim N(X_{f,t}, P_{f,t} + (Q - 1) \cdot \text{diag}(P_{f,t})) \\ Y_t &\sim N(X_A, R_t) \end{aligned} \quad (6)$$

where Q is the estimated forecast inflation scalar and X_A is a drawn sample from the analysis distribution. The estimation of X_A and Q was completed using a Markov chain Monte Carlo (MCMC) approach by leveraging the nimble R library (de Valpine et al., 2017, 2022). Though not explored in this study, this approach also allows for the definition and estimation of more complex relationships between observations and model forecasts (e.g., nonlinear observation operators).

In this study, the GEF was applied over the EnKF–Miyoshi workflow when (1) more than one observation was assimilated for a single state variable at a given time step or (2) the number of available observations varied throughout a simulation (i.e., changing H). Conversely, the GEF approach was ineffective for cases where only one observation was available at a given time step, as the MCMC algorithm did not converge due to limited data. The EnKF–Miyoshi was applied in these settings.

2.4.6 Simulation schemes

All simulations in this study were performed with 100 ensembles and with a 4-month initialization period starting on 1 January of the first year at each site. There were nine different simulations performed for each site in this study, which varied in terms of observations assimilated and assimilation method applied (Table 2). First, two “baseline” runs were completed across all 19 site years to establish system performance benchmarks. As a lower bound on performance, a free model simulation was performed with no data assimilation. SM sensor observations were also assimilated into the model to represent a reasonable benchmark data assimilation setting. Next, two groups of runs were performed to test the assimilation of RS SM data products: “individual” and “additive” runs. In the “individual” runs, all four RS data products were assimilated independently within the system. These runs were performed to compare the value of different RS data products directly. Then, in the “additive” runs, observations from multiple RS data products were jointly assimilated into the system following an additive approach. The first iteration included only ESA observations, and each subsequent iteration added another data product until all four data products were included (i.e., ALL). Data products were added in succession based on availability, such that the first data product tested had the highest average number of observations per year. By sequentially adding new data products, the additional impact of each RS data product could be evaluated. To allow for the application of the GEF in runs with more than one data product, a minimum of two observations per day were required for the “additive runs” to ensure the convergence of the MCMC algorithm. For all runs where RS data were assimilated, only site years after 2014 were investigated due to the limited temporal extent of RS data products.

2.5 System evaluation

This study applied the year-average ensemble weighting strategy, as presented in Kivi et al. (2022), to leverage all available information from the simulations and evaluate the results more accurately. In each site-year simulation, daily weights were assigned to each ensemble as the likelihood of producing the daily estimate given the analysis distribution, and ensemble weights were normalized across the model ensemble for each day. Finally, the average annual weight for each ensemble was computed for each site year. The application of annual weights in the analysis was the most robust for evaluating yearly estimates (e.g., yield, cumulative NO₃ load, cumulative tile drainage).

To evaluate the accuracy and precision of model forecasts for each site-year simulation, we utilized the root mean squared error (RMSE), spectral norm, and weighted variance. RMSE was calculated for each run to quantify changes in accuracy between runs, while the spectral norm

Table 2. Overview of system configuration for the nine runs performed in this study. SDA methods include the ensemble Kalman filter (EnKF) coupled with the Miyoshi algorithm and the generalized ensemble filter (GEF). The former method of these two methods provided systematic estimates of R applied within the system, but the latter method used literature values. The state variables included in X_f are given.

Run group	Name	SDA method	R estimates	Temporal extent	State variable(s)	Observation(s)
Baseline	Free	n/a	n/a	2011–2019	n/a	n/a
	SDA	EnKF	Miyoshi	2011–2019	SM3, SM4	In situ soil sensor
Individual runs	ESA	EnKF	Miyoshi	2015–2019	SM1	ESA
	SMAP–HB	EnKF	Miyoshi	2015–2019	SM1	SMAP–HB
	1 km*	EnKF	Miyoshi	2015–2019	SM1	1 km
	3 km*	EnKF	Miyoshi	2015–2019	SM1	3 km
Additive runs	+ SMAP–HB	GEF	Literature	2015–2019	SM1	ESA, SMAP–HB
	+ 1 km*	GEF	Literature	2015–2019	SM1	ESA, SMAP–HB, 1 km
	ALL*	GEF	Literature	2015–2019	SM1	ESA, SMAP–HB, 1, 3 km

* Observations for 1 and 3 km were not available for IL, and thus simulations were not performed for the site. n/a stands for not applicable.

and weighted variance were employed to quantify changes in precision. Additionally, to help standardize accuracy measures across site years, a normalized RMSE (nRMSE) was calculated as

$$\text{nRMSE}(\%) = 100 \cdot \frac{\text{RMSE}}{\bar{Y}}, \tag{7}$$

where \bar{Y} is the average observed value. Changes in accuracy and precision between the free model and SDA were quantified by computing the relative change in each metric for the two runs. For example, for calculating the change in RMSE, we computed

$$\Delta\text{RMSE} = \frac{\text{RMSE}_{\text{SDA}} - \text{RMSE}_{\text{FREE}}}{\text{RMSE}_{\text{FREE}}}. \tag{8}$$

The coefficient of determination (R^2) was used to compare model performance for each state variable more effectively across all observed time points. It was calculated as

$$R^2 = 1 - \frac{\sum_{t=1}^T (Y_t - \bar{X}_t)^2}{\sum_{t=1}^T (Y_t - \bar{X}_t)^2 + \sum_{t=1}^T (\bar{X}_t - \bar{Y})^2}, \tag{9}$$

where Y_t is the observed value at the t th observed time step and is the simulated weighted mean at the t th observed time step. All observations ($n = T$) from all site years were included in this calculation. Separate R^2 values were computed for the free and SDA results. Weighted mean estimates were computed using annual ensemble weights. In addition, spectral norm and weighted variance were estimated as follows:

$$\|P_f\|_2 = \sqrt{\text{maximum eigenvalue of } P_f^H P_f}, \tag{10}$$

where P_f^H represents the conjugate transpose of P_f .

$$\text{Variance} = \frac{\sum_{i=1}^N (w_i - (x_i - \bar{x}w))^2}{\frac{(N-1)}{N}}, \tag{11}$$

where N is the number of ensembles, w_i is the average weight of the i th ensemble, $\bar{x}w$ is the weighted mean across ensembles, and x_i is the forecasted value of the i th ensemble.

To identify and quantify relationships between variables, one of two correlation statistics was employed depending on the sample size of the data. When comparing data with a sufficiently large sample size ($n > 30$), the Pearson correlation coefficient (r) was calculated to determine the direction and strength of the linear relationship between two variables.

$$r = \frac{\sum_{i=1}^n (x_i - \bar{x})(y_i - \bar{y})}{\sqrt{\sum_{i=1}^n (x_i - \bar{x})^2} \cdot \sqrt{\sum_{i=1}^n (y_i - \bar{y})^2}} \tag{12}$$

When comparing data at the site level ($n \leq 19$), the Spearman rank-order correlation coefficient (r_s) was applied, which is a nonparametric measure of the strength and direction of the monotonic relationship between two variables. Though the sample size in this case is still too small for proper application, the Spearman coefficient was applied as its assumptions are less strict than the Pearson coefficient. It is calculated as

$$r_s = 1 - \frac{6 \sum_{i=1}^n d_i^2}{n(n^2 - 1)}, \tag{13}$$

where the d_i is the distance between the two ranks of the i th complete pair (i.e., x_i and y_i). For both coefficients, a test for association between paired samples was used to determine significance.

3 Results

The results in Sect. 3.1 evaluate the forecast accuracy and precision of in situ SM SDA in comparison to the free model. Section 3.2 investigates changes in forecast accuracy and precision when assimilating SM RS observations. The individual runs are assessed with regard to their data characteristics (i.e., retrieval interval and single vs. multi-sensor development), and the additive runs are evaluated in succession to determine the relative impact of added observations. Lastly, the impact of RS-based SDA on the forecast accuracy and precision of state variables is investigated and compared.

3.1 Assimilation of in situ soil moisture

3.1.1 Impact on soil moisture

Across all assimilation time steps, the free model tended to overpredict SM within the two assimilation layers (Fig. 3). Therefore, the adjustment in the SDA analysis step typically reduced the total amount of water in the soil profile. In SM forecasts for the two assimilation layers (i.e., SM3 and SM4), SDA performed as well or better than the free model in accuracy across all site years. The median change in RMSE due to SDA was -17% and -28% for SM3 and SM4, respectively (Fig. 4). Average forecast precision for SM3 and SM4 was also increased with SDA in 84% of cases and by 23% on average.

The three site years where precision was not increased in SDA include OH in 2013 and 2014 and MN in 2013. Interestingly, these site years were among those with the most remarkable improvement in accuracy. This relationship is intuitive considering the nature of the Miyoshi algorithm, which systematically inflates model forecast uncertainty at time steps when observed and forecasted SM distributions differ substantially. At the cost of reduced forecast precision, such inflation allows for the filter to pull the model forecast toward the observed distribution and improve accuracy in future predictions.

SDA's constraint of SM3 and SM4 also led to the indirect constraint of SM in deeper soil profile layers. Across all site years with available data, the median change in RMSE for SDA estimates of SM5, SM6, and SM7 was -14% , -8% , and -14% , respectively. In terms of precision, SDA had an overall positive impact on lower-layer SM estimates. The average change in weighted variance was -16% , -6% , and -20% for estimates of SM5, SM6, and SM7, respectively.

3.1.2 Impact on NDVI and crop yield

Overall, in comparison to the free model, SDA improved yield estimates by explaining 17.7% more variation in observed yield values and improving yield accuracy in 63% of site years (Table 3). SDA accuracy was most effective in site years facing greater water stress. In those cases where yield estimates were improved, SDA often increased available soil

water at critical points in crop development, reducing crop soil water deficit factors and increasing yield compared to the free model (Fig. A1). The most evident example of SDA yield improvement is IN in 2012, where the free model estimated complete maize crop failure (i.e., no grain yield) due to leaf senescence in mid-July, but SDA estimated a harvestable crop due to increased soil water in the early season (Fig. 5). However, SDA's impact on yield precision was inconsistent; roughly 53% of site years saw reduced precision in yield estimates.

Overall, the free model accurately captured the phenological development of the cropping systems simulated in this study, as demonstrated by the good agreement between observed and simulated NDVI (Fig. A2). SDA's impact on NDVI accuracy was similar to its impact on yield accuracy, such that it typically either increased accuracy due to lessened water stress or did not substantially affect the model performance. A comparison of R^2 values demonstrates that SDA helped to explain 4.8% more variation in observed NDVI values compared to the free model. Intuitively, the site years with the greatest jumps in NDVI accuracy also usually showed great improvement in yield accuracy, highlighting a well-defined physiological relationship between vegetation and grain yield in APSIM's maize and plant modules. SDA's impact on NDVI precision was inconsistent, such that 63% of site years reduced precision in estimates.

3.1.3 Impact on tile drainage and nitrate load

Across the 19 site years, the free model and SDA showed overall poor performance in estimating annual drainage with nRMSE values ranging from 18% – 215% with a median value of 54.3% for SDA and from 20% – 250% in the free model with a median value of 52.4% . In the site years with the lowest accuracy, APSIM often overpredicted drainage in both the free model and SDA. However, these cases of considerable overestimation in drainage were also among those site years that were most improved by SDA; 8 of the 11 site years where SDA improved estimates of annual drainage were cases where the free model overestimated tile flow. In these scenarios, SDA functioned to remove available water from the soil profile and correctly lower the amount of water lost from the system. In the remaining site years where SDA did not improve drainage accuracy, SDA increased RMSE values by 32% on average. SDA's impact on precision for annual drainage estimates was highly variable. A total of 63% of site years saw improvement in precision, but 4 site years saw an immense reduction in precision (i.e., between 107% – 146% reduction).

APSIM also struggled to accurately estimate the annual NO_3 load for the tested site years in this study (Fig. A3). For the free model, nRMSE values ranged from 23% – 681% with a median value of 83.7% , and for SDA nRMSE values ranged from 17% – 833% with a median value of 86.9% . Considering the SDA constraint, estimates of annual NO_3

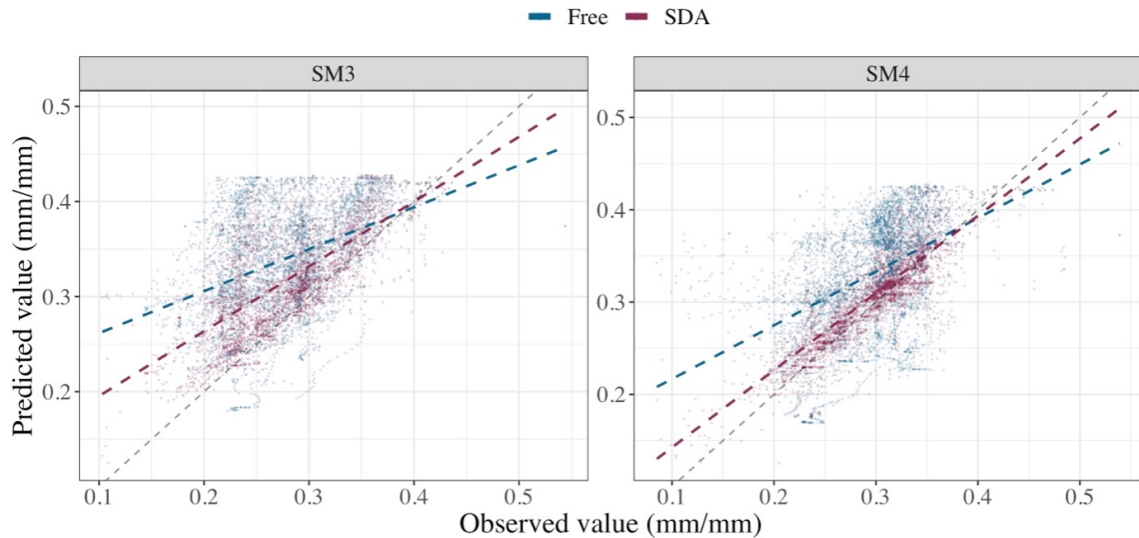


Figure 3. One-to-one plots for soil moisture estimates (mm mm^{-1}) in the two assimilation layers for the free model and in situ SDA across all analysis time steps and site years. The least-squares regression line is shown for both schemes next to the black dashed 1 : 1 line, demonstrating a perfect fit.

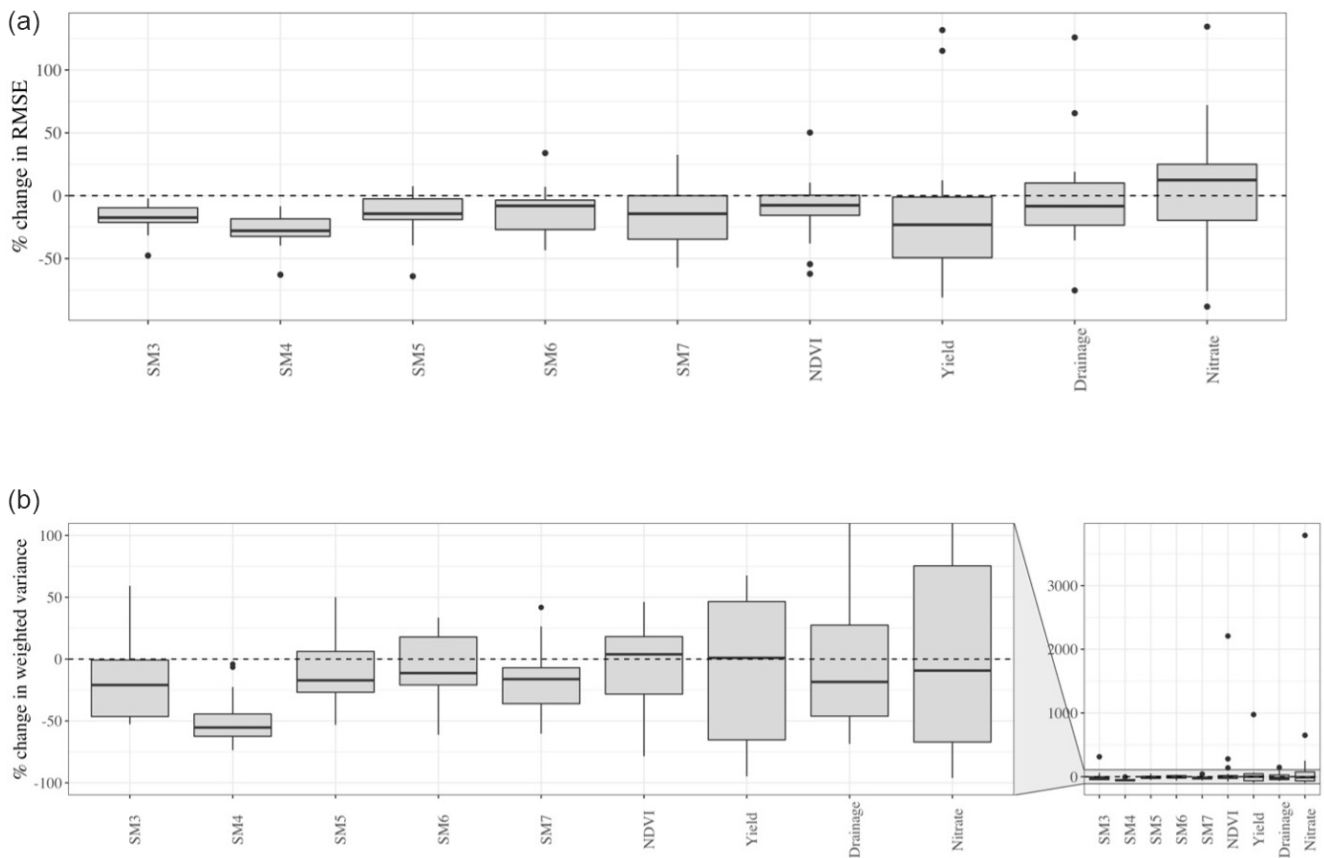


Figure 4. Boxplots demonstrating the distribution of relative change in (a) accuracy (RMSE) and (b) precision (weighted variance) due to in situ SDA for each state variable across all site years. The relative change is computed with respect to the free model run, with negative values indicating SDA improvement.

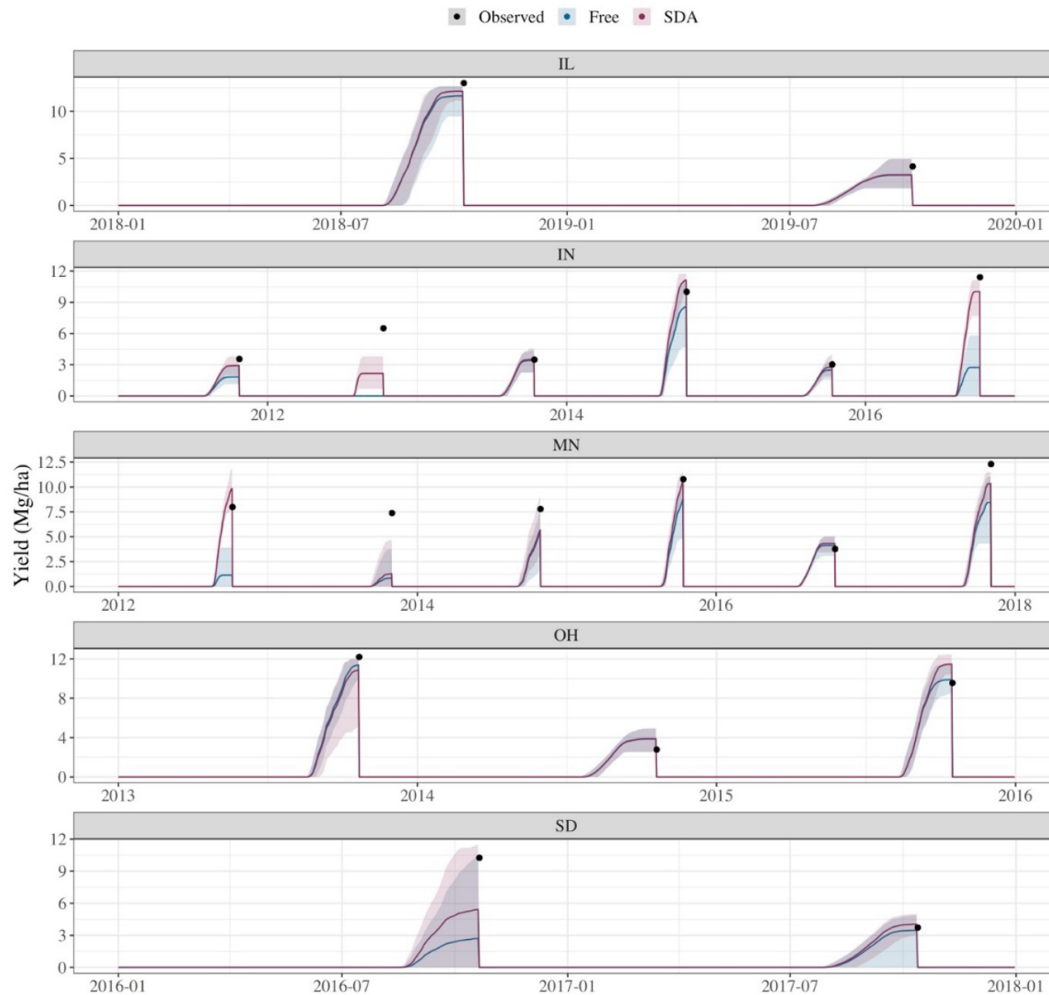


Figure 5. Time series of yield estimates for the free model and in situ SDA with mean daily estimates demonstrated with line graphs and the 95 % credible intervals demonstrated by the shaded regions. Black points represent the observed harvest date and yield for each site year.

load were the most poorly constrained in terms of accuracy and precision. SDA's impact on precision was split, increasing precision in 53 % of site years. Accuracy was improved for just 32 % of site years. Among those 6 site years where SDA increased NO_3 load accuracy, SDA typically reduced estimates compared to the free model. Improved sites were often maize years characterized by high-input winter precipitation (January–April). No clear environmental or agronomic trend was identified among those 11 site years in which SDA reduced accuracy.

3.2 Assimilation of remote sensing soil moisture products

3.2.1 Individual assimilation runs

As expected, the individual influence of each RS data product was heavily dependent on its multi- or single-sensor design and temporal availability. ESA, the most widely avail-

able data product, had the greatest impact on both assimilation and downstream state variables. In contrast, assimilation with 1 and 3 km imposed only slight changes in estimates when compared to the free model. However, ESA did not always lead to improvements in model performance. As demonstrated in Fig. 6, ESA results were more variable across site years in terms of the accuracy of state variable estimates, in some cases leading to great improvement and, in other cases, leading to reduced performance. ESA reduced accuracy in predicting SM3 and SM4 in most site years (i.e., 80 %–90 %) but was the most effective in improving accuracy in estimates of annual yield, SM6, and SM7. ESA also outperformed the other three RS data products in constraining forecast precision for all state variables, improving precision in 70 %–100 % of site years. Importantly, it showed the greatest reduction in the spectral norm of the SM covariance matrix when compared to the free model, indicating the best constraint of SM precision across the entire profile.

Table 3. Summary statistics to quantify the impact of in situ SDA (IS) and RS-SDA (RS) on forecast accuracy of APSIM state variables. The “ N_{IS} ” column indicates the number of site years with available data for each state variable and each run, and the “ n_{IS} ” column indicates the total number of observations across site years for each run. A subscript F denotes a value computed for the free model estimates, a subscript IS denotes a value for the in situ SDA estimates, and a subscript RS denotes a value for RS-SDA runs. The median change (D) in RMSE was computed for both runs. Two values for R2F are given for the different data subsets demonstrated in the “ N ” and “ n ” columns.

State variable	Depth (cm)	N_{IS} (N_{RS})	n_{IS} (n_{RS})	ΔRMSE_{IS}	ΔRMSE_{RS}	R_F^2	R_{IS}^2	R_{RS}^2
SM3 mm mm ⁻¹	9.1–16.6	19 (10)	12 252 (5592)	–17.4 %	–0.9 %	0.49 (0.48)	0.57	0.48
SM4 mm mm ⁻¹	16.6–28.9	19 (10)	12 735 (6141)	–27.9 %	–2.8 %	0.52 (0.43)	0.73	0.43
SM5 mm mm ⁻¹	28.9–49.3	17 (8)	11 325 (5101)	–14.3 %	–2.6 %	0.45 (0.45)	0.38	0.45
SM6 mm mm ⁻¹	49.3–82.9	19 (10)	12 846 (6169)	–8.0 %	–1.0 %	0.42 (0.43)	0.34	0.42
SM7 mm mm ⁻¹	82.9–138	9 (6)	5715 (3265)	–14.3 %	–5.4 %	0.43 (0.44)	0.34	0.43
NDVI unitless	–	19 (10)	244 (134)	–7.64 %	–1.8 %	0.62 (0.69)	0.66	0.71
Yield mg ha ⁻¹	–	19 (10)	19 (10)	–23.1 %	–17.2 %	0.55 (0.53)	0.73	0.59
Annual drainage mm	–	19	19	–8.3 %	–	0.47	0.46	–
Annual NO ₃ load kg NO ₃ -N ha ⁻¹	–	19	19	+12.5 %	–	0.42	0.45	–

Alternatively, the assimilation of SMAP–HB, another temporally frequent RS data product, demonstrated more conservative performance than ESA across state variables. For almost all state variables, it also performed similarly or better than the free model. However, any improvements (or reductions) in forecast accuracy were more moderate than observed with ESA. For example, accuracy in yield estimates was improved more consistently with SMAP–HB (90 %) compared to ESA (70 %), but the maximum improvement in a tested site year was a 53 % accuracy increase compared to a 95 % increase with ESA. This trend in the results highlights an important trade-off when assimilating more certain observations (i.e., ESA CCI) at a coarse spatial resolution over less certain observations at high spatial resolution (i.e., SMAP–HB) when both data products have unknown biases. In terms of forecast precision, SMAP–HB was overall quite effective in constraining state variable predictions, especially when compared to 1 and 3 km. However, SMAP–HB underperformed compared to ESA in this regard; 1 and 3 km both underperformed in accuracy constraint when compared to ESA and SMAP–HB, showing little to no change in RMSE compared to the free model.

Considering the four individual runs, more frequent assimilation time steps also led to a more robust performance of the EnKF–Miyoshi workflow. Filter divergence (i.e., when the observed mean falls outside of the 95 % credibility interval of the analysis distribution) occurred at 52 % and 59 % of analysis time steps for 1 and 3 km, respectively, but occurred at only 44 % and 30 % of analysis time steps for SMAP–HB and ESA, respectively. For estimates of observation uncertainty, the Miyoshi algorithm predicted greater uncertainty for most RS observations than what is reported in the literature. The average standard error in ESA observations was reported to be $0.02 \pm 0.004 \text{ mm}^3 \text{ mm}^{-3}$ but estimated in this study as $0.05 \pm 0.01 \text{ mm}^3 \text{ mm}^{-3}$. Standard errors in 1 and 3 km estimates were reported as $0.05 \text{ m}^3 \text{ m}^{-3}$ but estimated by the system to be 0.07 ± 0.02 and $0.06 \pm 0.01 \text{ mm}^3 \text{ mm}^{-3}$, respectively. Miyoshi estimated similar uncertainty values for SMAP–HB observations as reported in the literature (i.e., $0.07 \pm 0.02 \text{ mm}^3 \text{ mm}^{-3}$).

3.2.2 Additive runs

The baseline run for the additive RS-SDA runs was ESA, which demonstrated inconsistent constraint of forecast accuracy and strong constraint of forecast precision. The sec-

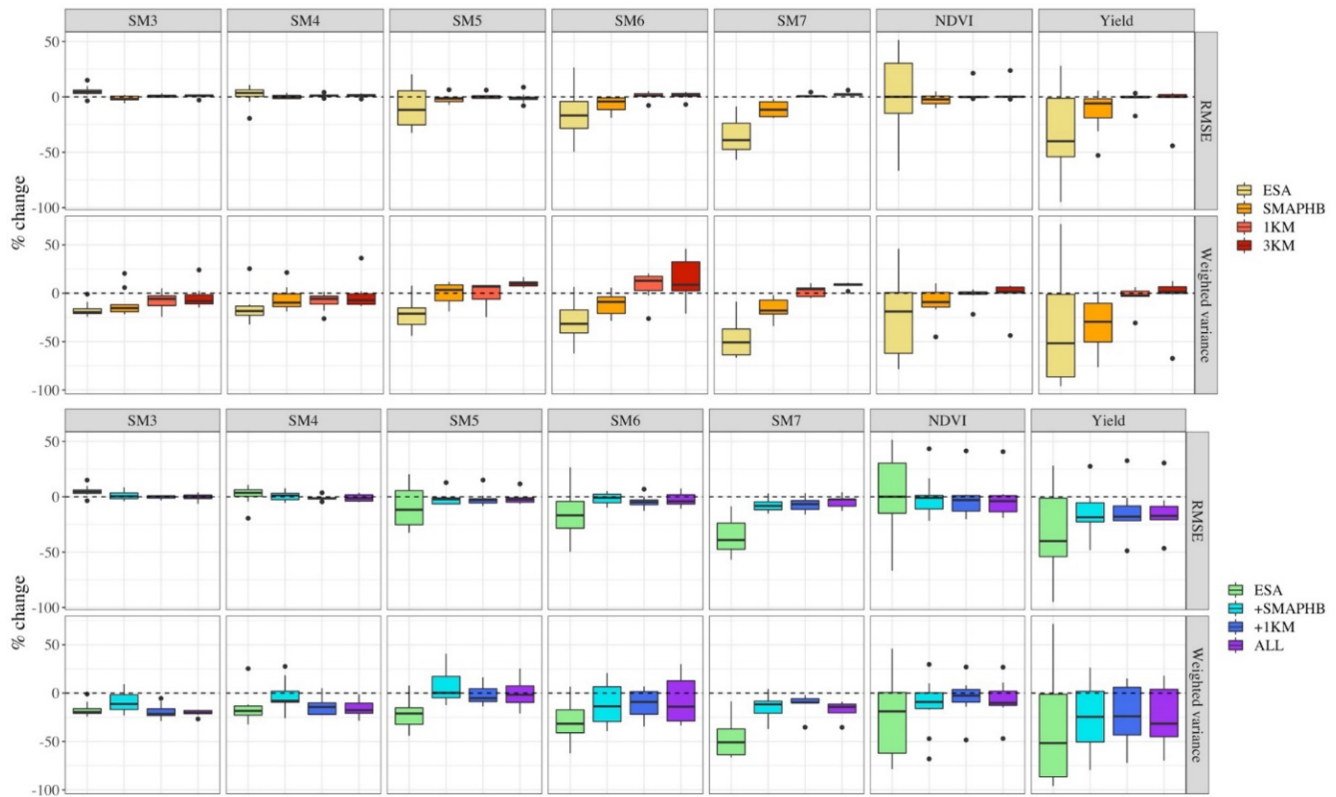


Figure 6. Boxplots demonstrating the distribution of relative change (%) in state variable accuracy (RMSE) and precision (weighted variance) for the (a) individual and (b) additive runs across all site years. Change is computed relative to the free model results. Negative values indicate improvement (e.g., $(RMSES - RMSEF)/RMSEF$).

ond most available data product, SMAP–HB, was the next RS data product added to the system. New SMAP–HB observations, on average, imposed a $-0.012 \text{ mm mm}^{-1}$ change in $-0.0003 \text{ mm mm}^{-1}$ and a -0.0003 change in Pa for SM1 estimates. For downstream forecast accuracy, the addition of SMAP–HB led to improved and/or more consistent constraints for all state variables except SM7 (Fig. 6). At times, the added information from SMAP–HB dampened the benefit of SDA, reducing accuracy improvement. For forecast precision, + SMAP–HB precision was overall better than the free model but with reduced performance compared to ESA.

The subsequent additions of the sparser 1 and 3 km RS data products were less impactful than the addition of SMAP–HB. New 1 km observations imposed an average $-0.0004 \text{ mm mm}^{-1}$ change in $\mu\alpha$ and, later, new 3 km observations imposed an average $-0.0003 \text{ mm mm}^{-1}$ change in $\mu\alpha$. These changes were less than 4% of the change imposed by the initial addition of SMAP–HB. Neither additional data product produced a notable average change in Pa. Following these minimal changes in SM1, there was also little change in forecast accuracy and precision for downstream state variables in +1 km and ALL when compared to + SMAP–HB (Fig. 6). Adding 1 km observations to

+ SMAP–HB did hold some benefit for accuracy and precision in SM3 and SM4, while the effect of the 3 km observations was almost negligible or, even at times, harmful to system performance.

3.2.3 Impact on APSIM model estimates

When considering the impact of surface SM data assimilation on downstream model variables, we focus on results where all available RS observations were assimilated for each site. Hereinafter, we refer to the compilation of these runs across the five sites as RS-SDA.

Overall, RS-SDA had minor impacts on the soil water profile relative to the free model. Figure 7 demonstrates differences between the free model and RS-SDA in SM1 estimates. For several site years, RS-SDA estimated significantly higher SM1 values in the early growing season (i.e., May–June). In the late season and fall, RS-SDA often estimated lower SM1 values. The impact of these SM1 changes on lower layer SM values seemed to decrease with depth, such that differences between the free model and RS-SDA mean estimates were more subtle in deeper layers. This reduced impact on lower layers is also, in part, a reflection of the increasing total soil water volume represented by soil lay-

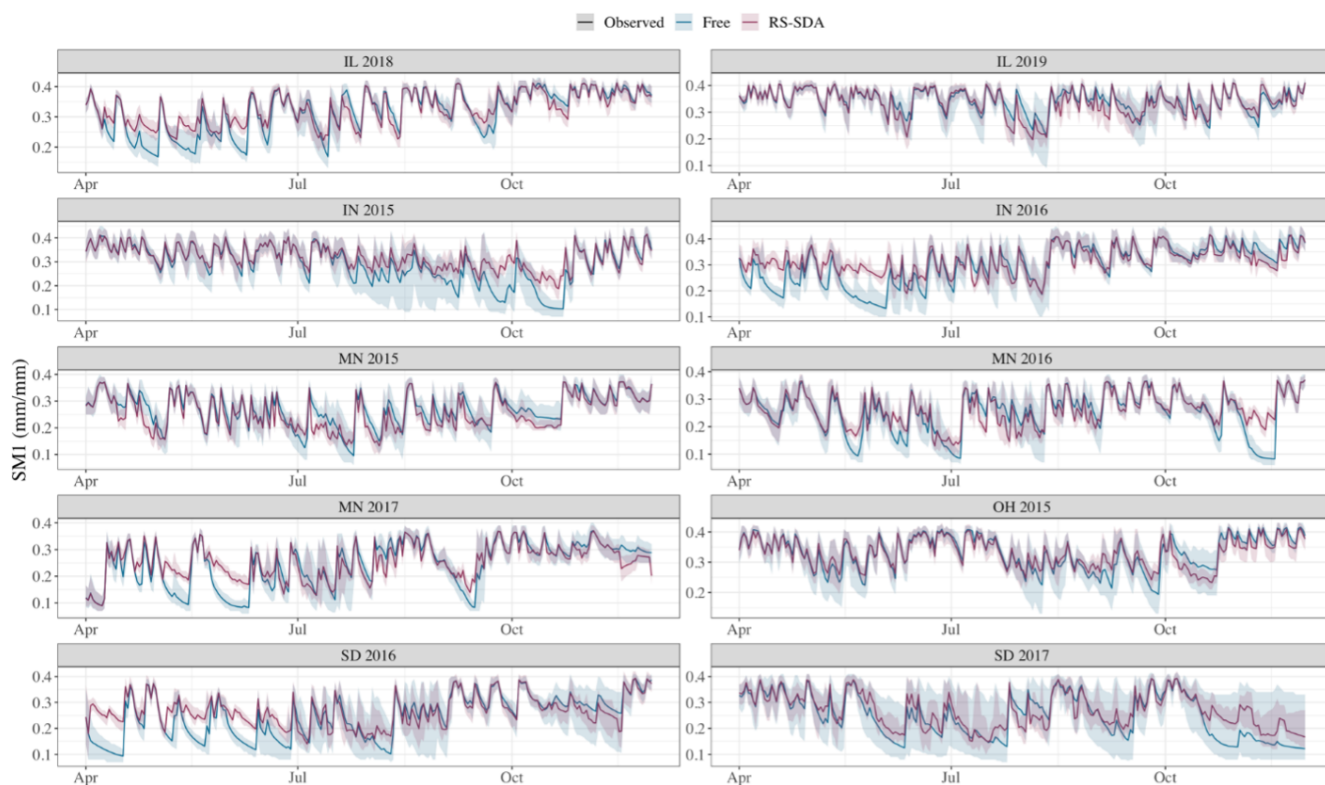


Figure 7. Time series of SM1 estimates from the free model and RS-SDA with the mean daily estimates demonstrated with line graphs. The shaded regions indicate 95 % credibility intervals.

ers down through the profile (see Table 3 for layer depths). Nonetheless, any differences in SM estimates did not lead to notable changes in accuracy for any SM layer (Table 3). Notable changes were visible in the soil water deficit factors for several growing seasons, such that RS-SDA led to reduced water stress for the growing crop. We speculate that this results from increased available soil water in the root zone during initial periods of crop water uptake (i.e., June). Forecast precision for soil-water-related estimates also did not change substantially with assimilation. For SM1 estimates, assimilation substantially reduced variability across site years (Fig. 7). In many cases, this constraint in the surface soil layer did not propagate into significant changes for precision in lower layer estimates (Fig. 7). However, on average, precision was improved rather than reduced with assimilation, with the most significant downstream constraint in the soil layers closest to the surface.

RS-SDA demonstrated partial constraint of aboveground estimates. Considering the R^2 values reported in Table 3, RS-SDA explained roughly 4 % more variation in yield observations than the free model. All site years except OH 2015 demonstrated increased yield accuracy, and 60 % of sites demonstrated increased yield precision with RS-SDA. Based on these results, there is evidence that surface SM data assimilation can constrain, to some extent, estimates of annual

yield. Compared to its effect on yield estimates, RS-SDA was less impactful in its constraint of NDVI. However, since the free model could reasonably predict NDVI ($R^2 = 0.69$), there was less potential for improvement with SM assimilation. A total of 60 % of site years had increased accuracy, and 70 % had increased precision for NDVI estimates following SDA.

4 Discussion

4.1 Sensitivity of APSIM model estimates to in situ soil moisture

In this study, the extent to which in situ SM data assimilation affected APSIM model predictions depended on each state variable's sensitivity to the assimilated state variable (i.e., soil moisture). Deeper layer SM estimates – the most sensitive state variables to SM3 and SM4 – were the most strongly constrained. Figure A1 demonstrates the significant linear relationship between daily changes in forecasted SM3 and SM4 due to SDA and daily changes in SM estimates for all deeper soil layers. As expected with a cascading water balance model, the strength of the linear relationship weakens as the vertical distance between soil layers increases. In the model, SM in each layer can influence SM estimates

of deeper soil layers, but only indirectly through its influence on the SM in the layer immediately below it. Therefore, the influence of the assimilation layers is reduced by each subsequent SM process down through the soil profile and is weakest in the final soil layer (SM7). Nevertheless, the constraint of SM7 was still quite strong in SDA. By assimilating SM for two upper soil layers, the accuracy of SM estimates improved immensely by simply leveraging the pre-existing model structure (compare to Liu et al., 2017).

Crop yield showed the next strongest constraint in SDA. However, as noted in previous studies, its sensitivity to SM SDA was conditional (Lu et al., 2021; Kivi et al., 2022). While changes in SM affected lower layer SM at all analysis time steps, crop yield was only affected when the changes impacted crop water stress. Daily crop water uptake is determined in APSIM as the minimum of crop water demand and soil water supply. Therefore, SDA could only influence crop yield when the soil water adjustment pushed the water supply above or below the demand threshold. For this reason, greater SDA improvement was found in crop yield estimates during water-stressed site years. Other pathways through which SM can impact crop yield in APSIM, like soil N cycling, did not play a strong role in this study.

The impact of SM SDA on APSIM drainage estimates can also be beneficial, given certain conditions. As shown in the results, drainage was affected by SM3 and SM4 through two pathways: (1) changes in total soil water with assimilation adjustment and (2) changes in crop water uptake due to changes in crop water stress. The role of each of these pathways varied over the year, such that the presence of a growing crop and root system weakened the sensitivity of drainage estimates to changes in the assimilation layers. To quantify this change in sensitivity, we divided daily model forecasts into two categories: with crop water uptake (June–September) and without crop water uptake. Then, the relationship between changes in SM3 and SM4 and changes in drainage was analyzed separately for each group. There was no significant linear relationship when looking at SM3 changes in either case. However, the linear relationship between changes in SM4 and changes in daily drainage was stronger when no crop was present ($r = 0.23$, $p = 0.00$) than when a crop was present ($r = 0.14$, $p = 0.00$). This is similar to Hu et al. (2008), who identified notable changes in drainage dynamics during rapid crop growth compared to out-of-season dynamics in SPWS model simulations.

Among the state variables considered in SDA, NO_3 leaching showed the weakest and most complex relationship with SM3 and SM4 in APSIM. Therefore, logically, the presented system performed most poorly in its constraint of annual NO_3 leaching estimates. In APSIM, daily NO_3 leaching estimates are computed as the product of two different daily values: estimated NO_3 concentration in the lowest soil layer and estimated tile drainage. Therefore, in addition to its impact on drainage, SDA can affect NO_3 load estimates through (1) changes in N cycle processes via SM rate factors

(see Fig. 2 in Kivi et al., 2022) and (2) changes in the vertical movement of soil water (and N solutes) through the soil profile. In a validation study of APSIM N processes, Sharp et al. (2011) also observed inconsistent model behavior in annual leaching estimates for their experimental site in New Zealand when simulating three years of a potato–rye rotation. Their final calibration of the model only improved one of the annual estimates but did not constrain estimates in the other two years. In fact, many past studies have highlighted nitrate leaching estimates as a broader forecasting challenge (Stewart et al., 2006; Sharp et al., 2011; van der Laan et al., 2014; Brilli et al., 2017). As highlighted already in the literature, missing processes related to snowmelt (Ojeda et al., 2018), tillage-related infiltration (Malone et al., 2007; Brilli et al., 2017; Ojeda et al., 2018), or preferential flow could help to improve APSIM performance. Though there is still potential for the presented system to improve nitrate leaching estimates, further investigation and constraint of the APSIM N and soil water cycles will be necessary to ensure consistent performance.

4.2 Impact of remote sensing soil moisture data assimilation

The assimilation of RS surface SM observations imposed a far weaker constraint on APSIM state variables compared to the assimilation of the soil sensor observations. For example, the median reduction in SM RMSE ranged from 7%–27% across different layers of the soil profile with soil sensor observations, but, with RS observations in RS-SDA, it ranged from roughly 1%–5% (Table 3). The weakened constraint with RS-SDA was likely more than an issue of observation inaccuracies. Instead, there is greater evidence to show that changes in SM1 simply had less influence on downstream state variables than changes in SM3 and SM4. This is due, in part, to the increased vertical distance between the surface SM layer (SM1) and other observed soil layers (i.e., SM3–7). The APSIM SoilWat module operates as a cascading water balance model to estimate the movement of water and solutes between and across soil layers (Dokoochaki et al., 2018). Thus, the assimilation adjustment of the SM1 estimate would not be as strongly tied to lower layer estimates when using a top-down approach. Yet, surface SM data assimilation notably changed SM2 estimates, the SM estimates for the layer just below it. This result reflects the findings of Lu and et al. (2019), who assimilated RS surface SM observations into a surface energy balance model. They found that SDA improved SM estimates in the second layer to a greater extent than in lower layers when comparing estimates to observations. Since observations were not available for SM2 at the study sites, this hypothesis could not be tested within this work.

The two assimilation protocols (i.e., assimilation of SM1 vs. assimilation of SM3 and SM4) were also markedly different in the quantity of soil water associated with their assim-

ilation adjustments. Where soil layers 3 and 4 corresponded to almost 14 % of the soil profile (20 cm depth), the near-surface soil layer only corresponded to about 3.6 % of the soil profile (5 cm depth). Thus, when considering the top-down effect of SM assimilation on lower layers, each adjustment with RS assimilation had just 25 % of the impact of the previous system given the same adjustment in volumetric soil water content. This 5-fold reduction in potential impact closely mirrors the change in RMSE reduction for SM layers highlighted above (i.e., 7 %–27 % to 1 %–5 %). One way to overcome this limitation of surface SM is to leverage the strong covariance between SM1 and SM in nearby layers (i.e., SM2) to directly nudge their values within the analysis time step using, for example, an augmented state vector (e.g., Kivi et al., 2022) or exponential filter approaches (e.g., Albergel et al., 2008).

RS surface SM data assimilation still demonstrated strong potential for improving APSIM forecasts within this study. First, the assimilation of surface SM improved estimates of crop yield overall when compared to the free model, with a median RMSE reduction of 17.2 %. Past RS SM data assimilation studies had similar success in improving crop yield estimates, and several attributed the improvement to increased surface SM and reduced crop water stress with SM assimilation (e.g., Ines et al., 2013; Chakrabarti et al., 2014). We speculate that the model performance indicates that water stress likely played an important role. Although direct observations are not available for crop water uptake to test this hypothesis, we suspect RS-SDA accurately increased available soil water at critical growth stages and, thus, increased crop water uptake.

4.3 Comparison of remote sensing soil moisture data products

The four different RS SM data products varied quite broadly in spatial resolution, varying from 30 m to 0.25°. However, their individual assimilation performance seemed to be most closely tied to the temporal availability of observations. ESA with a multi-sensor nature had on average 219 observations per growing season and showed the best overall constraint of forecast precision and good constraint of forecast accuracy in downstream state variables. Alternatively, the 1 and 3 km data products, which each had an average of seven observations per growing season, had almost no impact on forecast accuracy and only a slight impact on forecast precision. Although this study was not designed to independently test the impact of temporal and spatial resolution on performance, it echoes the findings of Lu et al. (2019), who found a high temporal resolution to be far more important to assimilation performance than high spatial resolution. They suspected that increased time between assimilation adjustments allowed errors in model structure, inputs, and/or parameters to go unchecked for more extended periods of time, thereby allowing the magnitude of simulation errors to be-

come large and unreasonable. More frequent assimilation helps mitigate the impact of such model errors and improve overall crop model predictions by correcting errors more often (de Lannoy et al., 2007; Pauwels et al., 2007; Lu et al., 2021). Alternatively, in the case of low temporal resolution, a recalibration-based assimilation approach or the inclusion of a bias correction method might be more appropriate (de Lannoy et al., 2007; Curnel et al., 2011).

When comparing RS data products in this study, it is important to recognize that all data products considered in this work are based, in part, on SMAP radiometer data. SMAP–HB merged SMAP brightness temperature data with the HydroBlocks–RTM model, ESA includes SMAP as one of its 10 passive microwave sensors, and 1 and 3 km rely on SMAP for passive microwave information within their derivation. In the first iteration, ESA contributed most of the information provided by the SMAP radiometer to the model and, therefore, imposed large changes in SM1 estimates. Then, with each additional data product, the overall impact on the analysis distribution weakened, as much of the new information had already been provided to the system. It is also important to note that given that all data products directly or indirectly are based SMAP, the successive assimilation of these data products can introduce error covariances between the model runs and the observations. This may potentially result in an over- or underestimation of the uncertainty, thereby affecting the performance of the filter. Therefore, further investigation into the impact of including these error covariances between the data products is deemed necessary in order to enhance the accuracy of the EnKF filter.

The Miyoshi algorithm often estimated higher observation uncertainty (R) than the values reported in the literature. This is unsurprising as RS SM data products, like most RS data products, often have poorly characterized uncertainties (Peng et al., 2021). For each data product, uncertainty is typically reported as a standard error value after comparing the data product to a limited set of observations. This estimate does not capture all possible sources of uncertainty and cannot be easily generalized to different places or time points (Huang et al., 2019). Yet, in the additive runs, these uncertainty values were applied uniformly across time and space. Future applications of the GEF scheme could benefit from additional terms in the model that could capture R or the use of the Miyoshi algorithm. These approaches may better estimate observation uncertainties within the system's context.

5 Conclusions

In the study, we assessed the extent to which soil moisture data assimilation can improve APSIM model forecasts. We used a generalizable and novel data-assimilation system to assimilate RS and in situ soil moisture measurements across the US Midwest 19 site years and evaluated how a direct soil moisture constraint affected downstream model estimates of

root zone soil moisture, crop yield, tile flow, and nitrate leaching. Our results highlighted the capacity of soil moisture data assimilation to improve model estimates of crop yield in water-limited conditions, increasing crop water uptake at critical points in the growing season. Soil moisture data assimilation also improved estimates of soil moisture throughout the profile in most cases but did not well constrain nitrate leaching or tile drainage. This indicates a need for better constraint of both the soil water and soil nitrogen cycles in the APSIM model.

This work also lays the groundwork for future regional applications of soil moisture data assimilation. Importantly, our findings reaffirmed soil moisture data assimilation's ability to "localize" gridded weather estimates of precipitation to reflect observed values more accurately. Since cropping systems are highly sensitive to precipitation inputs, this is a strong advantage of soil moisture data assimilation for forecasting applications where coarse-resolution weather drivers are employed. Though RS soil moisture data assimilation could be an effective way to overcome limited availability of in situ data, our work shows that assimilation of in situ surface soil moisture is not as powerful as the assimilation of in situ root zone soil moisture values in terms of model constraint. If the former is applied, additional constraints or an augmented state-vector approach would be necessary to achieve higher system performance. When selecting a RS soil moisture data product for data assimilation applications, high temporal resolution due to multi-sensor satellite availability and accurately estimated observation uncertainty are two critical components for optimal system performance. To that same point, combining several data products at different spatial resolutions can help to reduce assimilation intervals within the system. Further investigation is needed to independently test the impact of observation sample size (i.e., number of data products), temporal resolution, spatial resolution, and uncertainty on system performance. Moreover, the data products considered in this study do not represent the full range of RS soil moisture data products that are available publicly. This work should be expanded to evaluate data products derived from other satellites/derivations both individually and in combination with other sources to exhaust all available options.

Appendix A

Table A1. Site management information as defined across all APSIM simulations in this study.

Study ID (original ID)	Site information	Year	Crop	Planting date	Harvest date	Tillage	Fertilizer ^c
IL (Energy Farm)	plot ID: maize control soy cultivar: 3.5–4.5 tile depth: 1.383 m	2018	maize	8 May	9 Oct	8 May: chisel 50 mm ^a 24 Oct: chisel 150 mm	8 May: urea_N (101) NH ₄ NO ₃ (288.57)
		2019	soy	17 May	9 Oct	n/a	n/a
			2011	soy	7 Jun	24 Oct	n/a
IN (IN_Randolph)	plot ID: SW soy cultivar: 3.0–4.0 tile depth: 0.975 m ^b	2012	maize	23 Apr	10 Oct	12 Apr: disk 50 mm ^a 28 Nov: disk 200 mm	13 Feb: NH ₄ _N (22.42) broadcast_P (46.25) 23 Apr: urea_N (17.88) NH ₄ NO ₃ (51.09) banded_P (13.96) 25 May: urea_N (100.35) NH ₄ NO ₃ (286.7)
		2013	soy	20 May	14 Oct	9 Apr: disk 50 mm ^a 21 Oct: chisel 150 mm	21 Mar: NH ₄ _N (18.48) broadcast_P (38.12)
		2014	maize	27 Apr	21 Oct	13 Nov: chisel 150 mm	24 Apr: NH ₄ _N (17.93) broadcast_P (36.99) 23 Apr: urea_N (17.88) NH ₄ NO ₃ (51.09) banded_P (13.96) 25 May: urea_N (108.82) NH ₄ NO ₃ (310.9)
		2015	soy	6 Jun	12 Oct	n/a	n/a
IN (cont.)		2016	maize	26 Apr	7 Oct	n/a	26 Apr: urea_N (16.71) NH ₄ NO ₃ (47.73) banded_P (13.05) 2 Jun: urea_N (104.91) NH ₄ NO ₃ (299.7)
MN (MN_Redwood1)	plot ID: BE soy cultivar: 1.5–2.5 tile depth: 1.22 m	2012	maize	10 May	6 Oct	6 May: disk 76.2 mm ^a 1 Nov: rip 228.6 mm	6 May: urea_N (177.1) NH ₄ _N (13.4) broadcast_P (34.2) 10 May: NH ₄ _N (7.84) banded_P (76.2)
		2013	maize	24 May	31 Oct	23 May: disk 76.2 mm ^a 3 Nov: rip 228.6 mm	22 May: urea_N (182.75) NH ₄ _N (13.4) broadcast_P (34.2) 24 May: NH ₄ _N (7.84) banded_P (11.63)
		2014	maize	17 May	29 Oct	16 May: disk 76.2 mm ^a 1 Nov: rip 228.6 mm	16 May: urea_N (150.47) NH ₄ _N (12.05) broadcast_P (30.8) 17 May: NH ₄ _N (7.84) banded_P (11.63)
		2015	maize	30 Apr	13 Oct	29 Apr: disk 50.8 mm ^a 27 Oct: rip 228.6 mm	28 Apr: urea_N (148.37) NH ₄ _N (14.15) broadcast_P (18.6) 1 May: NH ₄ NO ₃ (47.8) urea_N (16.49)

Table A1. Continued.

Study ID (original ID)	Site information	Year	Crop	Planting date	Harvest date	Tillage	Fertilizer ^c
MN (cont.)		2016	soy	13 May	18 Oct	11 May: disk 50.8 mm ^a 1 Nov: rip 228.6 mm	n/a
		2017	maize	6 May	3 Nov	6 May: disk 50.8 mm ^a	6 May: NH ₄ _N (7.84) broadcast_P (11.63)
OH (OH_Auglaize2)	plot ID: WS soy cultivar: 3.0–4.0 tile depth: 0.975 m ^b	2013	maize	9 May	22 Oct	n/a	9 May: broadcast_P (20.53) NH ₄ _N (11.76) urea_N (201.43)
		2014	soy	15 May	20 Oct	5 Nov: disk 200 mm	n/a
		2015	maize	30 Apr	16 Oct	n/a	30 Apr: NH ₄ _N (18.38) broadcast_P (38.12) urea_N (178.76)
SD (SD_Clay)	plot ID: Plot7 soy cultivar: 2.0–3.0 tile depth: 1.22 m	2016	maize	18 May	21 Oct	15 May: disk 101.6 mm ^a	14 Apr: urea_N (180.32)
		2017	soy	2 Jun	13 Oct	n/a	n/a

^a Documentation on site-level management indicated the use of a field cultivator during spring tillage for several site years. However, since the APSIM tillage module does not include parameterization for a field cultivator, the disk implement was applied at the documented depth instead due to similarities between the two implements in relation to incorporation. ^b OH and IN both fall within the same tile of the gridded soil driver. Therefore, since the drainage tiles were placed at similar depths at the two sites (i.e., 0.91 and 1.04 m), the soil profile depth was adapted to the average depth of the two for simplicity. ^c This column includes information on fertilizer application date, type, and amount as defined for each site year. The notation for fertilizer type reflects fertilizer names in APSIM. If the fertilizer name contains N or P, amount is in kg N ha⁻¹ or Kg P ha⁻¹, respectively. Otherwise, amount is in kg per fertilizer per ha. n/a stands for not applicable. n/a stands for not applicable.

Table A2. Prior distributions for model ensembles.

APSIM variable	Description	Units	Distribution
iCRAG	Initial residue weight on the field	kg	Uniform (0, 2500)
water_fraction_full	Initial soil water fraction by volume	Proportion	Uniform (0.05, 0.6)
tt_flower_to_maturity	Thermal time between flowering and maturity (maize cultivar)	°C d ⁻¹	Uniform (780, 860)
tt_flower_to_start_grain	Thermal time between flowering and start of grain fill (maize cultivar)	°C d ⁻¹	Uniform (150, 200)
tt_maturity_to_ripe	Thermal time between maturity and ripe stage (maize cultivar)	°C d ⁻¹	Uniform (150, 250)
tt_emerg_to_endjuv	Thermal time between emergence and end of juvenile stage (maize cultivar)	°C d ⁻¹	Uniform (240, 260)
head_grain_no_max	Maximum potential number of kernels per ear (maize cultivar)	Number of kernels per ear	Uniform (750, 900)
grain_gth_rate	Maximum potential growth rate of grain (maize cultivar)	Grain (g) per day	Uniform (7.1, 8.57)

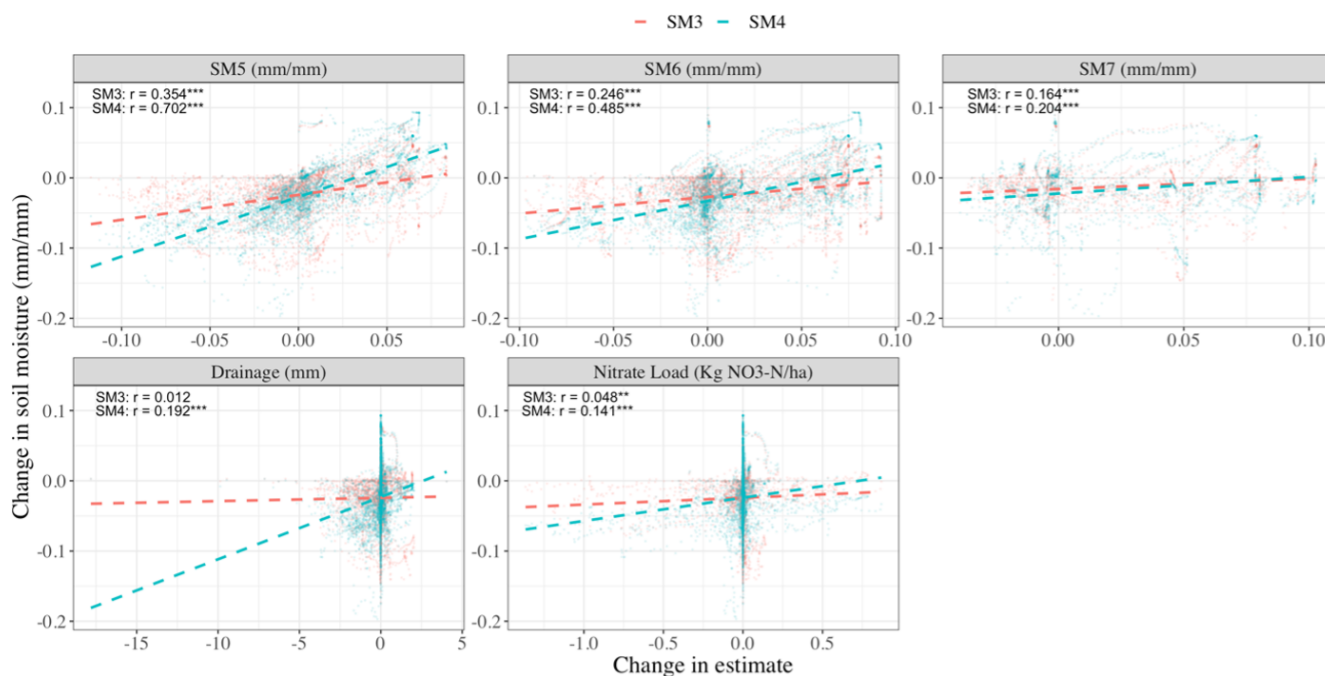


Figure A1. Scatterplots comparing change (i.e., SDA – free model) in mean SM5, SM6, SM7, daily drainage, and daily NO₃ leaching estimates with change in mean SM3 and SM4 estimates at each analysis time step. For each variable combination, the least squares regression line is demonstrated by a dashed line and the Pearson correlation coefficient is displayed. Asterisks denote significant coefficient values (** indicates p value < 0.01, and *** indicates p value ~ 0).

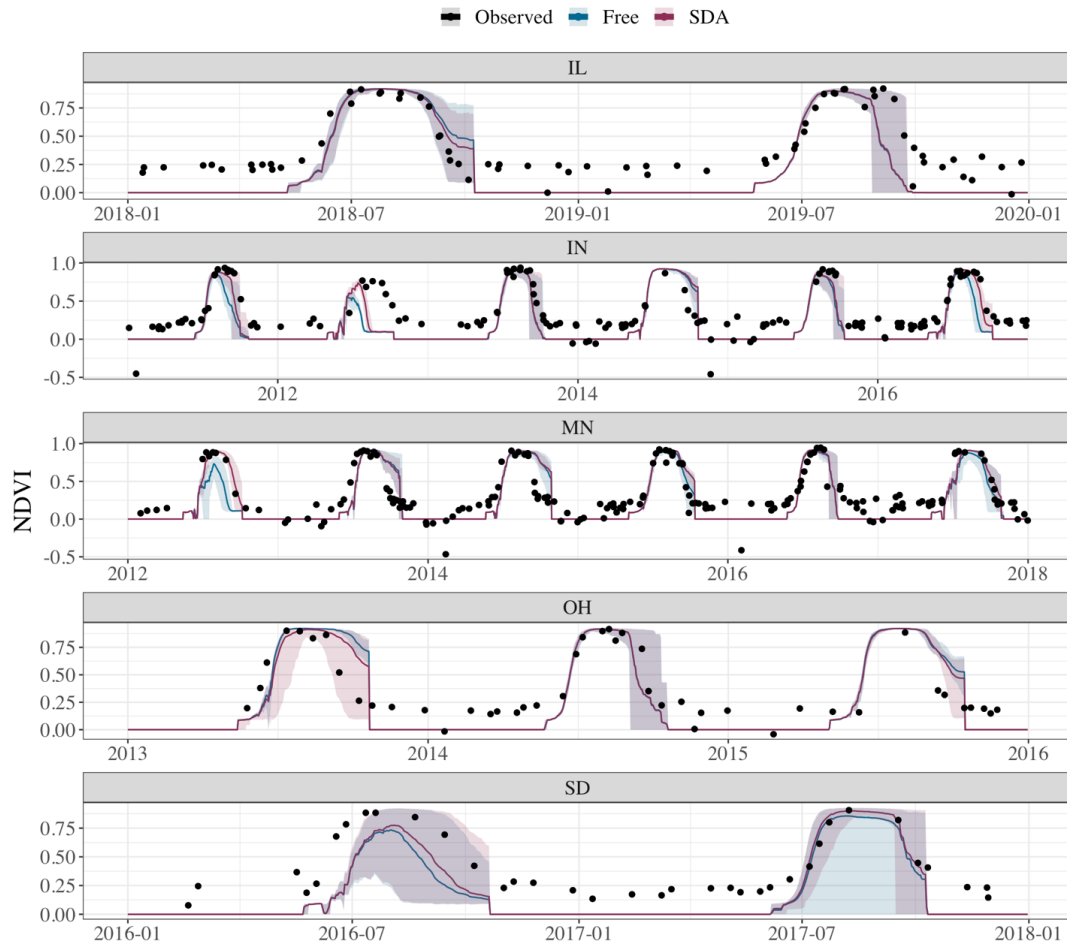


Figure A2. Time series of NDVI estimates from the two schemes for each site year with the mean daily estimates demonstrated with line graphs and the 95 % credibility interval demonstrated by the shaded regions. Black points represent the observed values.

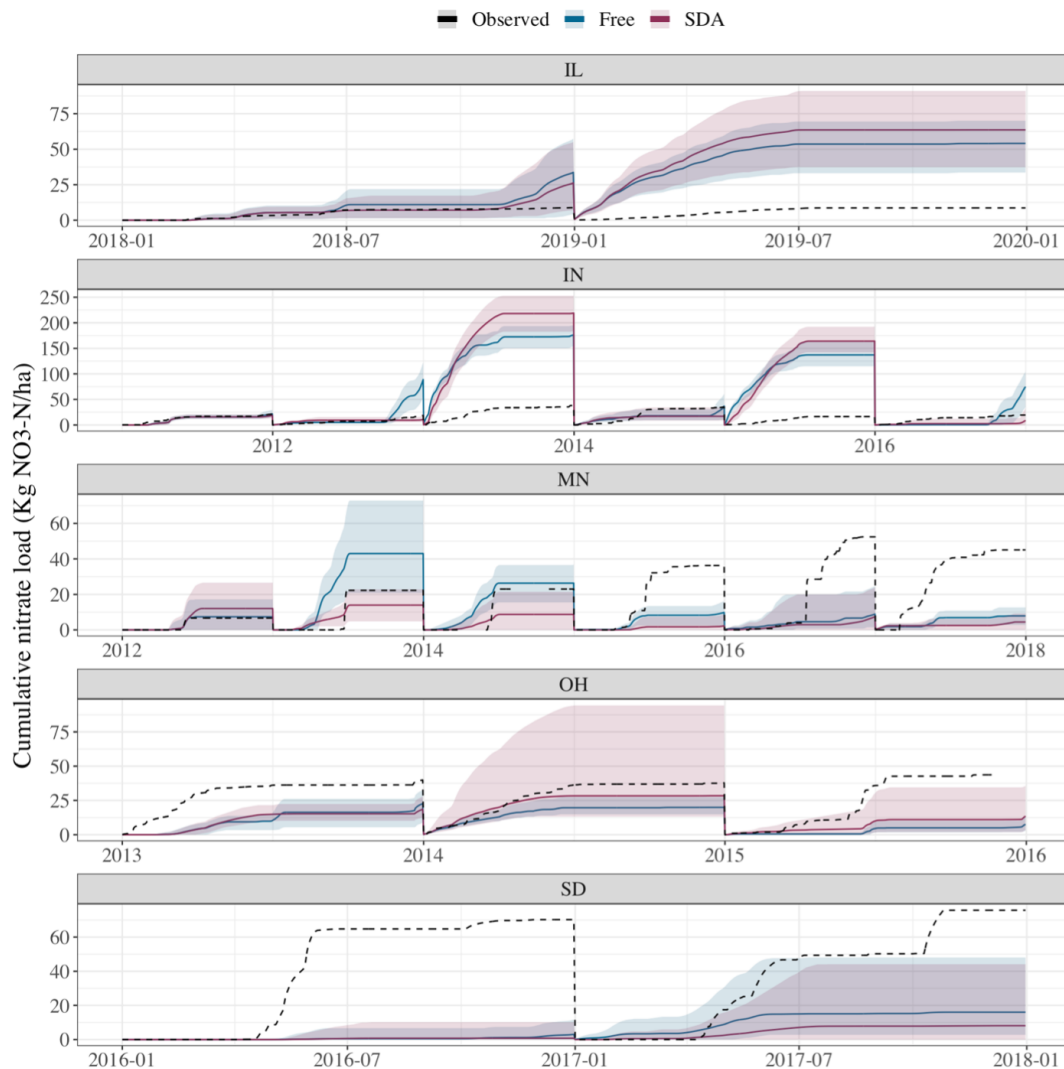


Figure A3. Time series of cumulative NO_3 load estimates from the two schemes for each site year with the mean daily estimates demonstrated with line graphs and the 95 % credibility interval demonstrated by the shaded regions. Black dashed lines represent the observed cumulative value for each site year.

Code and data availability. Code and observational data used in this study will be provided upon request.

Author contributions. MK was responsible for code development, performing the simulations, and writing the manuscript. NV contributed to revising the manuscript and provided the SMAP-HB dataset. HD was responsible for developing the initial idea, code development, writing, and supervising the study.

Competing interests. The contact author has declared that none of the authors has any competing interests.

Disclaimer. Publisher's note: Copernicus Publications remains neutral with regard to jurisdictional claims in published maps and institutional affiliations.

Acknowledgements. The authors would like to thank all those on the Energy Farm team who made the presented case study possible. In particular, we would like to thank Carl Bernacchi, Bethany Blakely, Michael Masters, Grace Andrews, and Heather Goring-Harford, who made the Energy Farm dataset available and performed the analyses for the nitrate leaching data, and Konrad Taube and Haley Ware, who helped with water collection and water filtering in 2018 and 2019. We also want to thank Caitlin Moore and Evan Dracup, who helped to collect and process much of the other data from the plot. Additionally, we wanted to acknowledge those funding sources that supported the work of the

Energy Farm team. First, the data used in this study were funded in part by (1) the Leverhulme Centre for Climate Change Mitigation, funded by the Leverhulme Trust through a Research Centre award (RC-2015-029); (2) the Center for Advanced Bioenergy and Bioproducts Innovation (CABBI) at the University of Illinois; and (3) the Global Change and Photosynthesis Research Unit of the USDA Agricultural Research Service.

Review statement. This paper was edited by Alexander Gruber and reviewed by Warrick Dawes and Svitlana Kokhan.

References

- Albergel, C., Rüdiger, C., Pellarin, T., Calvet, J.-C., Fritz, N., Froissard, F., Suquia, D., Petitpa, A., Pignatelli, B., and Martin, E.: From near-surface to root-zone soil moisture using an exponential filter: an assessment of the method based on in-situ observations and model simulations, *Hydrol. Earth Syst. Sci.*, 12, 1323–1337, <https://doi.org/10.5194/hess-12-1323-2008>, 2008.
- Brilli, L., Bechini, L., Bindi, M., Carozzi, M., Cavalli, D., Conant, R., Dorich, C. D., Doro, L., Ehrhardt, F., Farina, R., Ferrise, R., Fitton, N., Francaviglia, R., Grace, P., Iocola, I., Klumpp, K., Léonard, J., Martin, R., Massad, R. S., Recous, S., Seddaiu, G., Sharp, J., Smith, P., Smith, W. N., Soussana, J.-F., and Bellocchi, G.: Review and analysis of strengths and weaknesses of agro-ecosystem models for simulating C and N fluxes, *Sci. Total Environ.*, 598, 445–470, <https://doi.org/10.1016/j.scitotenv.2017.03.208>, 2017.
- Chakrabarti, S., Bongiovanni, T., Judge, J., Zotarelli, L., and Bayer, C.: Assimilation of SMOS soil moisture for quantifying drought impacts on crop yield in agricultural regions, *IEEE J. Select. Top. Appl.*, 7, 3867–3879, <https://doi.org/10.1109/JSTARS.2014.2315999>, 2014.
- Chen, Y., Zhang, Z., and Tao, F.: Improving regional winter wheat yield estimation through assimilation of phenology and leaf area index from remote sensing data, *Eur. J. Agron.*, 101, 163–173, <https://doi.org/10.1016/j.eja.2018.09.006>, 2018.
- Chighladze, G., Abendroth, L. J., Herzmann, D., Helmers, M., Ahiablame, L., Allred, B., Bowling, L., Brown, L., Fausey, N., Frankenberger, J., Jaynes, D., Jia, X., Kjaersgaard, J., King, K., Kladvik, E., Nelson, K., Pease, L., Reinhart, B., Strock, J., and Youssef, M.: Transforming Drainage Research Data (USDA-NIFA Award No. 2015-68007-23193), National Agricultural Library – ARS – USDA, <https://doi.org/10.15482/USDA.ADC/1521092>, 2021.
- Crow, W. T., Berg, A. A., Cosh, M. H., Loew, A., Mohanty, B. P., Panciera, R., de Rosnay, P., Ryu, D., and Walker, J. P.: Upscaling sparse ground-based soil moisture observations for the validation of coarse-resolution satellite soil moisture products: UPSCALING SOIL MOISTURE, *Rev. Geophys.*, 50, RG2002, <https://doi.org/10.1029/2011RG000372>, 2012.
- Curnel, Y., de Wit, A. J. W., Duveiller, G., and Defourny, P.: Potential performances of remotely sensed LAI assimilation in WOFOST model based on an OSS Experiment, *Agr. Forest Meteorol.*, 151, 1843–1855, <https://doi.org/10.1016/j.agrformet.2011.08.002>, 2011.
- Das, N. N., Entekhabi, D., Dunbar, R. S., Chaubell, M. J., Collander, A., Yueh, S., Jagdhuber, T., Chen, F., Crow, W., O'Neill, P. E., Walker, J. P., Berg, A., Bosch, D. D., Caldwell, T., Cosh, M. H., Collins, C. H., Lopez-Baeza, E., and Thibeault, M.: The SMAP and Copernicus Sentinel 1A/B microwave active-passive high resolution surface soil moisture product, *Remote Sens. Environ.*, 233, 111380, <https://doi.org/10.1016/j.rse.2019.111380>, 2019.
- de Lannoy, G. J. M., Houser, P. R., Pauwels, V. R. N., and Verhoest, N. E. C.: State and bias estimation for soil moisture profiles by an ensemble Kalman filter: Effect of assimilation depth and frequency, *Water Resour. Res.*, 43, W06401, <https://doi.org/10.1029/2006WR005100>, 2007.
- de Valpine, P., Turek, D., Paciorek, C., Anderson-Bergman, C., Temple Lang, D., and Bodik, R.: Programming with models: writing statistical algorithms for general model structures with NIMBLE, *J. Comput. Graph. Stat.*, 26, 403–413, <https://doi.org/10.1080/10618600.2016.1172487>, 2017.
- de Valpine, P., Paciorek, C., Turek, D., Michaud, N., Anderson-Bergman, C., Obermeyer, F., Wehrhahn Cortes, C., Rodriguez, A., Temple Lang, D., and Paganin, S.: NIMBLE: MCMC, Particle Filtering, and Programmable Hierarchical Modeling, doi:10.5281/zenodo.1211190, R package version 0.12.2, <https://cran.r-project.org/package=nimble> (last access: October 2021), 2022.
- de Wit, A. J. W. and van Diepen, C. A.: Crop model data assimilation with the Ensemble Kalman filter for improving regional crop yield forecasts, *Agr. Forest Meteorol.*, 146, 38–56, 2007.
- Dietze, M.: Ecological Forecasting, Princeton University Press, Princeton, <https://doi.org/10.1515/9781400885459>, 2017.
- Dokoohaki, H., Miguez, F. E., Archontoulis, S., and Laird, D.: Use of inverse modelling and Bayesian optimization for investigating the effect of biochar on soil hydrological properties, *Agr. Water Manage.*, 208, 268–274, 2018.
- Dokoohaki, H., Kivi, M. S., Martinez-Feria, R., Miguez, F. E., and Hoogenboom, G.: A comprehensive uncertainty quantification of large-scale process-based crop modeling frameworks, *Environ. Res. Lett.*, 16, 084010, <https://doi.org/10.1088/1748-9326/ac0f26>, 2021.
- Dokoohaki, H., Morrison, B. D., Raiho, A., Serbin, S. P., Zarada, K., Dramko, L., and Dietze, M.: Development of an open-source regional data assimilation system in PEcAn v. 1.7.2: application to carbon cycle reanalysis across the contiguous US using SIPNET, *Geosci. Model Dev.*, 15, 3233–3252, <https://doi.org/10.5194/gmd-15-3233-2022>, 2022a.
- Dokoohaki, H., Rai, T., Kivi, M., Lewis, P., Gomez-Dans, J., and Yin, F.: Linking Remote Sensing with APSIM through Emulation and Bayesian Optimization to Improve Maize Yield Prediction in the US Midwest, *Remote Sens.*, 14, 5389, <https://doi.org/10.3390/rs14215389>, 2022b.
- Dorigo, W., Wagner, W., Albergel, C., Albrecht, F., Balsamo, G., Brocca, L., Chung, D., Ertl, M., Forkel, M., Gruber, A., Haas, E., Hamer, P. D., Hirschi, M., Ikonen, J., de Jeu, R., Kidd, R., Lahoz, W., Liu, Y. Y., Miralles, D., Lecomte, P., ESA CCI Soil Moisture for improved Earth system understanding: State-of-the-art and future directions, *Remote Sens. Environ.*, 203, 185–215, <https://doi.org/10.1016/j.rse.2017.07.001>, 2017.
- Dorigo, W. A., Zurita-Milla, R., de Wit, A. J. W., Brazile, J., Singh, R., and Schaepman, M. E.: A review on reflective re-

- remote sensing and data assimilation techniques for enhanced agroecosystem modelling, *Int. J. Appl. Earth Obs.*, 9, 165–193, <https://doi.org/10.1016/j.jag.2006.05.003>, 2007.
- Evensen, G.: The Ensemble Kalman Filter: theoretical formulation and practical implementation, *Ocean Dynam.*, 53, 343–367, <https://doi.org/10.1007/s10236-003-0036-9>, 2003.
- Fer, I., Gardella, A. K., Shiklomanov, A. N., Campbell, E. E., Cowdery, E. M., De Kauwe, M. G., Desai, A., Duveneck, M. J., Fisher, J. B., Haynes, K. D., Hoffman, F. M., Johnston, M. R., Kooper, R., LeBauer, D. S., Mantooh, J., Parton, W. J., Poulter, B., Quaipe, T., Raiho, A., and Dietze, M. C.: Beyond ecosystem modeling: A roadmap to community cyberinfrastructure for ecological data-model integration, *Global Change Biol.*, 27, 13–26, <https://doi.org/10.1111/gcb.15409>, 2021.
- Folberth, C., Skalský, R., Moltchanova, E., Balkovič, J., Azevedo, L. B., Obersteiner, M., and Van Der Velde, M.: Uncertainty in soil data can outweigh climate impact signals in global crop yield simulations, *Nat. Commun.*, 7, 11872, <https://doi.org/10.1038/ncomms11872>, 2016.
- Gao, F. and Zhang, X.: Mapping Crop Phenology in Near Real-Time Using Satellite Remote Sensing: Challenges and Opportunities, *J. Remote Sens.*, 2021, 1–14, <https://doi.org/10.34133/2021/8379391>, 2021.
- Helmerts, M. J., Abendroth, L., Reinhart, B., Chighladze, G., Pease, L., Bowling, L., Youssef, M., Ghane, E., Ahiablame, L., Brown, L., Fausey, N., Frankenberger, J., Jaynes, D., King, K., Kladienko, E., Nelson, K., and Strock, J.: Impact of controlled drainage on subsurface drain flow and nitrate load: A synthesis of studies across the U.S. Midwest and Southeast, *Agr. Water Manage.*, 259, 107265, <https://doi.org/10.1016/j.agwat.2021.107265>, 2022.
- Hengl, T., de Jesus, J. M., MacMillan, R. A., Batjes, N. H., Heuvelink, G. B. M., Ribeiro, E., Samuel-Rosa, A., Kempen, B., Leenaars, J. G. B., Walsh, M. G., and Gonzalez, M. R.: SoilGrids1km – Global Soil Information Based on Automated Mapping, *PloS ONE*, 9, e105992, <https://doi.org/10.1371/journal.pone.0105992>, 2014.
- Hersbach, H., Bell, B., Berrisford, P., Hirahara, S., Horányi, A., Muñoz-Sabater, J., Nicolas, J., Peubey, C., Radu, R., Schepers, D., Simmons, A., Soci, C., Abdalla, S., Abellan, X., Balsamo, G., Bechtold, P., Biavati, G., Bidlot, J., Bonavita, M., and Thépaut, J.: The ERA5 global reanalysis, *Q. J. Roy. Meteorol. Soc.*, 146, 1999–2049, <https://doi.org/10.1002/qj.3803>, 2020.
- Hu, K., Li, B., Chen, D., Zhang, Y., and Edis, R.: Simulation of nitrate leaching under irrigated maize on sandy soil in desert oasis in Inner Mongolia, China, *Agr. Water Manage.*, 95, 1180–1188, <https://doi.org/10.1016/j.agwat.2008.05.001>, 2008.
- Huang, J., Ma, H., Su, W., Zhang, X., Huang, Y., Fan, J., and Wu, W.: Jointly Assimilating MODIS LAI and ET Products Into the SWAP Model for Winter Wheat Yield Estimation, *IEEE J. Select. Top. Appl.*, 8, 4060–4071, <https://doi.org/10.1109/JSTARS.2015.2403135>, 2015.
- Huang, J., Gómez-Dans, J. L., Huang, H., Ma, H., Wu, Q., Lewis, P. E., Liang, S., Chen, Z., Xue, J.-H., Wu, Y., Zhao, F., Wang, J., and Xie, X.: Assimilation of remote sensing into crop growth models: Current status and perspectives, *Agr. Forest Meteorol.*, 276–277, 107609, <https://doi.org/10.1016/j.agrformet.2019.06.008>, 2019.
- Ines, A. V. M., Das, N. N., Hansen, J. W., and Njoku, E. G.: Assimilation of remotely sensed soil moisture and vegetation with a crop simulation model for maize yield prediction, *Remote Sens. Environ.*, 138, 149–164, <https://doi.org/10.1016/j.rse.2013.07.018>, 2013.
- Jacquemoud, S., Verhoef, W., Baret, F., Bacour, C., Zarco-Tejada, P. J., Asner, G. P., François, C., and Ustin, S. L.: PROSPECT+SAIL models: A review of use for vegetation characterization, *Remote Sens. Environ.*, 113, S56–S66, 2009.
- Kivi, M. S., Blakely, B., Masters, M., Bernacchi, C. J., Miguez, F. E., and Dokoohaki, H.: Development of a data-assimilation system to forecast agricultural systems: A case study of constraining soil water and soil nitrogen dynamics in the APSIM model, *Sci. Total Environ.*, 820, 153192, <https://doi.org/10.1016/j.scitotenv.2022.153192>, 2022.
- Kumar, S. V., Dirmeyer, P. A., Peters-Lidard, C. D., Bindlish, R., and Bolten, J.: Information theoretic evaluation of satellite soil moisture retrievals, *Remote Sens. Environ.*, 204, 392–400, <https://doi.org/10.1016/j.rse.2017.10.016>, 2018.
- Lehnert, L. W., Meyer, H., Obermeier, W. A., Silva, B., Regeling, B., Thies, B., and Bendix, J.: Hyperspectral Data Analysis in R: The hsdar Package, *J. Stat. Softw.*, 89, 1–23, <https://doi.org/10.18637/jss.v089.i12>, 2019.
- Lievens, H., Reichle, R. H., Liu, Q., De Lannoy, G. J. M., Dunbar, R. S., Kim, S. B., Das, N. N., Cosh, M., Walker, J. P., and Wagner, W.: Joint Sentinel-1 and SMAP data assimilation to improve soil moisture estimates, *Geophys. Res. Lett.*, 44, 6145–6153, <https://doi.org/10.1002/2017GL073904>, 2017.
- Linker, R. and Ioslovich, I.: Assimilation of canopy cover and biomass measurements in the crop model AquaCrop, *Biosyst. Eng.*, 162, 57–66, <https://doi.org/10.1016/j.biosystemseng.2017.08.003>, 2017.
- Liu, Y., Wang, W., and Hu, Y.: Investigating the impact of surface soil moisture assimilation on state and parameter estimation in SWAT model based on the ensemble Kalman filter in upper Huai River basin, *J. Hydrol. Hydromech.*, 65, 123–133, <https://doi.org/10.1515/johh-2017-0011>, 2017.
- Liu, Y., Wang, W., and Liu, Y.: ESA CCI Soil Moisture Assimilation in SWAT for Improved Hydrological Simulation in Upper Huai River Basin, *Adv. Meteorol.*, 2018, 1–13, <https://doi.org/10.1155/2018/7301314>, 2018.
- Liu, Z., Xu, Z., Bi, R., Wang, C., He, P., Jing, Y., and Yang, W.: Estimation of Winter Wheat Yield in Arid and Semiarid Regions Based on Assimilated Multi-Source Sentinel Data and the CERES-Wheat Model, *Sensors*, 21, 1247, <https://doi.org/10.3390/s21041247>, 2021.
- Lu, Y., Dong, J., and Steele-Dunne, S. C.: Impact of Soil Moisture Data Resolution on Soil Moisture and Surface Heat Flux Estimates through Data Assimilation: A Case Study in the Southern Great Plains, *J. Hydrometeorol.*, 20, 715–730, <https://doi.org/10.1175/JHM-D-18-0234.1>, 2019.
- Lu, Y., Chibarabada, T. P., Ziliani, M. G., Onema, J. M. K., McCabe, M. F., and Sheffield, J.: Assimilation of soil moisture and canopy cover data improves maize simulation using an under-calibrated crop model, *Agr. Water Manage.*, 252, 106884, <https://doi.org/10.1016/j.agwat.2021.106884>, 2021.
- Luce, G. A.: Optimum corn planting depth – Don't plant your corn too shallow, 6 April 2016, University of Missouri Integrated Pest and Crop Management, https://ipm.missouri.edu/cropPest/2016/4/Optimum_Corn_Planting_Depth-Dont_Plant_Your_

- Corn_Too_Shallow#:~:text=Checkplantingdepthwhenstarting, safeandsuccessfulplantingseason (last access: May 2021), 2016.
- Ma, G., Huang, J., Wu, W., Fan, J., Zou, J., and Wu, S.: Assimilation of MODIS-LAI into the WOFOST model for forecasting regional winter wheat yield, *Math. Comput. Model.*, 58, 634–643, <https://doi.org/10.1016/j.mcm.2011.10.038>, 2013.
- Malone, R. W., Huth, N., Carberry, P. S., Ma, L., Kaspar, T. C., Karlen, D. L., Meade, T., Kanwar, R. S., and Heilman, P.: Evaluating and predicting agricultural management effects under tile drainage using modified APSIM, *Geoderma*, 140, 310–322, <https://doi.org/10.1016/j.geoderma.2007.04.014>, 2007.
- Mishra, V., Cruise, J. F., and Mecikalski, J. R.: Assimilation of coupled microwave/thermal infrared soil moisture profiles into a crop model for robust maize yield estimates over Southeast United States, *Eur. J. Agron.*, 123, 126208, <https://doi.org/10.1016/j.eja.2020.126208>, 2021.
- Miyoshi, T., Kalnay, E., and Li, H.: Estimating and including observation-error correlations in data assimilation, *Inverse Probl. Sci. Eng.*, 21, 387–398, <https://doi.org/10.1080/17415977.2012.712527>, 2013.
- Monsivais-Huertero, A., Graham, W. D., Judge, J., and Agrawal, D.: Effect of simultaneous state–parameter estimation and forcing uncertainties on root-zone soil moisture for dynamic vegetation using EnKF, *Adv. Water Resour.*, 33, 468–484, <https://doi.org/10.1016/j.advwatres.2010.01.011>, 2010.
- Moore, C. E., Haden, A. C., Burnham, M. B., Kantola, I. B., Gibson, C. D., Blakely, B. J., Dracup, E. C., Masters, M. D., Yang, W. H., DeLucia, E. H., and Bernacchi, C. J.: Ecosystem-scale biogeochemical fluxes from three bioenergy crop candidates: How energy sorghum compares to maize and miscanthus, *GCB Bioenergy*, 13, 445–458, <https://doi.org/10.1111/gcbb.12788>, 2021.
- Mourtzinis, S. and Conley, S. P.: Delineating Soybean Maturity Groups across the United States, *Agron. J.*, 109, 1397–1403, <https://doi.org/10.2134/agronj2016.10.0581>, 2017.
- Naz, B. S., Kurtz, W., Montzka, C., Sharples, W., Goergen, K., Keune, J., Gao, H., Springer, A., Hendricks Franssen, H.-J., and Kollet, S.: Improving soil moisture and runoff simulations at 3 km over Europe using land surface data assimilation, *Hydrol. Earth Syst. Sci.*, 23, 277–301, <https://doi.org/10.5194/hess-23-277-2019>, 2019.
- Nearing, G. S., Crow, W. T., Thorp, K. R., Moran, M. S., Reichle, R. H., and Gupta, H. V.: Assimilating remote sensing observations of leaf area index and soil moisture for wheat yield estimates: An observing system simulation experiment, *Water Resour. Res.*, 48, W05525, <https://doi.org/10.1029/2011WR011420>, 2012.
- Ojeda, J. J., Volenec, J. J., Brouder, S. M., Caviglia, O. P., and Agnusdei, M. G.: Modelling stover and grain yields, and subsurface artificial drainage from long-term corn rotations using APSIM, *Agr. Water Manage.*, 195, 154–171, <https://doi.org/10.1016/j.agwat.2017.10.010>, 2018.
- Pauwels, V. R. N., Verhoest, N. E. C., De Lannoy, G. J. M., Guissard, V., Lucau, C., and Defourny, P.: Optimization of a coupled hydrology-crop growth model through the assimilation of observed soil moisture and leaf area index values using an ensemble Kalman filter: Assimilation Of LAI And Soil Moisture, *Water Resour. Res.*, 43, W04421, <https://doi.org/10.1029/2006WR004942>, 2007.
- Peng, J., Loew, A., Merlin, O., and Verhoest, N. E. C.: A review of spatial downscaling of satellite remotely sensed soil moisture: Downscale Satellite-Based Soil Moisture, *Rev. Geophys.*, 55, 341–366, <https://doi.org/10.1002/2016RG000543>, 2017.
- Peng, J., Albergel, C., Balenzano, A., Brocca, L., Cartus, O., Cosh, M. H., Crow, W. T., Dabrowska-Zielinska, K., Dadson, S., Davidson, M. W. J., de Rosnay, P., Dorigo, W., Gruber, A., Hagemann, S., Hirschi, M., Kerr, Y. H., Lovergine, F., Mahecha, M. D., Marzahn, P., Mattia, F., Musial, J. P., Preuschmann, S., Reichle, R. H., Satalino, G., Silgram, M., van Bodegom, P. M., Verhoest, N. E. C., Wagner, W., Walker, J. P., Wegmüller, U., and Loew, A.: A roadmap for high-resolution satellite soil moisture applications – confronting product characteristics with user requirements, *Remote Sens. Environ.*, 252, 112162, <https://doi.org/10.1016/j.rse.2020.112162>, 2021.
- Raiho, A., Dietze, M., Dawson, A., Rollinson, C. R., Tipton, J., and McLachlan, J.: Towards understanding predictability in ecology: A forest gap model case study, *Ecology*, <https://doi.org/10.1101/2020.05.05.079871>, in press, 2020.
- Sharp, J. M., Thomas, S. M., and Brown, H. E.: A validation of APSIM nitrogen balance and leaching predictions, *Agronomy New Zealand*, 12 pp., https://www.agronomysociety.org.nz/uploads/94803/files/2011_7_A_validation_of_APSIM.pdf (last access: May 2021), 2011.
- Silva, J. V. and Giller, K. E.: Grand challenges for the 21st century: What crop models can and can't (yet) do, *J. Agr. Sci.*, 158, 794–805, <https://doi.org/10.1017/S0021859621000150>, 2021.
- Staton, M.: Pay close attention to soybean planting depth, 9 May 2012, Michigan State University Extension, https://www.canr.msu.edu/news/pay_close_attention_to_soybean_planting_depth#:~:text=Neverplantssoybeanseeddeeper,theocotyledonsabovethesoil (last access: May 2021), 2012.
- Stewart, L. K., Charlesworth, P. B., Bristow, K. L., and Thorburn, P. J.: Estimating deep drainage and nitrate leaching from the root zone under sugarcane using APSIM-SWIM, *Agr. Water Manage.*, 81, 315–334, <https://doi.org/10.1016/j.agwat.2005.05.002>, 2006.
- van der Laan, M., Annandale, J. G., Bristow, K. L., Stirzaker, R. J., du Preez, C. C., and Thorburn, P. J.: Modelling nitrogen leaching: Are we getting the right answer for the right reason?, *Agr. Water Manage.*, 133, 74–80, <https://doi.org/10.1016/j.agwat.2013.10.017>, 2014.
- Vergopolan, N., Chaney, N. W., Beck, H. E., Pan, M., Sheffield, J., Chan, S., and Wood, E. F.: Combining hyper-resolution land surface modeling with SMAP brightness temperatures to obtain 30-m soil moisture estimates, *Remote Sens. Environ.*, 242, 111740, <https://doi.org/10.1016/j.rse.2020.111740>, 2020.
- Vergopolan, N., Xiong, S., Estes, L., Wanders, N., Chaney, N. W., Wood, E. F., Konar, M., Caylor, K., Beck, H. E., Gatti, N., Evans, T., and Sheffield, J.: Field-scale soil moisture bridges the spatial-scale gap between drought monitoring and agricultural yields, *Hydrol. Earth Syst. Sci.*, 25, 1827–1847, <https://doi.org/10.5194/hess-25-1827-2021>, 2021a.
- Vergopolan, N., Chaney, N. W., Pan, M., Sheffield, J., Beck, H. E., Ferguson, C. R., Torres-Rojas, L., Sadri, S., and Wood, E. F.: SMAP-HydroBlocks, a 30-m satellite-based soil moisture dataset for the conterminous US, *Scient. Data*, 8, 264, <https://doi.org/10.1038/s41597-021-01050-2>, 2021b.
- Weiss, M., Jacob, F., and Duveiller, G.: Remote sensing for agricultural applications: A meta-review, *Remote Sens. Environ.*, 236, 111402, <https://doi.org/10.1016/j.rse.2019.111402>, 2020.

Zhou, H., Wu, J., Li, X., Geng, G., and Liu, L.: Improving soil moisture estimation by assimilating remotely sensed data into crop growth model for agricultural drought monitoring, in: 2016 IEEE International Geoscience and Remote Sensing Symposium (IGARSS), 10–15 July 2016, Beijing, China, 4229–4232 <https://doi.org/10.1109/IGARSS.2016.7730102>, 2016.

Zhu, P., Shi, L., Zhu, Y., Zhang, Q., Huang, K., and Williams, M.: Data assimilation of soil water flow via ensemble Kalman filter: Infusing soil moisture data at different scales, *J. Hydrol.*, 555, 912–925, <https://doi.org/10.1016/j.jhydrol.2017.10.078>, 2017.